

# Extensional fracture network attribute distribution in faulted thick sandstone strata: Compione Fault, Northern Apennines, Italy

Alessio Lucca<sup>1</sup>, Fabrizio Storti<sup>1</sup>, Giancarlo Molli<sup>1,2</sup>

<sup>1</sup>NEXT - Natural and Experimental Tectonics research group, Department of Chemistry, Life Sciences and Environmental Sustainability, University of Parma, I-43124 Parma, Italy

<sup>2</sup>Department of Earth Sciences, University of Pisa, via S. Maria, 53, I-56126 Pisa, Italy

\*Corresponding Author Details

E-mail: alessio.lucca@studenti.unipr.it

Telephone number: +39 393 1323420

## Abstract

Intensely fractured rock volumes characterize fault damage zones in cohesive rocks and typically developed from multiple deformation stages associated with fault propagation and linkage. Despite many discussed implications for fluid flow, the connectivity of fault damage zones, which is fundamental to better understand their hydrogeological behavior, has been rarely quantified. In this paper, we report on results from a study performed to characterize the fracture pattern in thick sandstone strata in the footwall of the Compione active extensional fault zone. Fracture network attributes were studied in cross-sectional vertical exposures by the window sampling method, which allows to describe fracture topology, intensity, frequency, and orientations. Our data indicate that fracture network topology in the damage zone is dominated by Y- and X-nodes ( $Y > 55\%$  and  $20\% < X < 35\%$  of nodes) and by C-C branches ( $> 85\%$  of branches) in 5 out of 6 structural sectors going away from the fault core. Fractures are mainly composed by passively rotated and sheared, early conjugate subsidiary extensional faults, overprinted by late high-angle conjugate extensional faults, with fracture intensity logarithmically increasing towards the fault core. This study is a first attempt to quantify cross-fault connectivity of fault-related fractures using circular windows on vertical exposures.

## 1. Introduction

Regional-scale fault damage zones in cohesive rocks are typically characterized by complex fracture networks mainly resulting from (i) long lasting deformation histories including fault

32 nucleation, propagation, slip accumulation and linkage of adjacent segments; (ii) the mechanical  
33 stratigraphy of faulted rocks; (iii) the environmental conditions of deformation (Chester et al., 1993;  
34 Caine et al., 1996; Faulkner et al., 2010). Understanding the evolution of fracture networks in  
35 damage zones and quantifying their main attributes bears fundamental implications for making  
36 reliable predictions of fluid flow and storage in aquifers and hydrocarbon reservoirs, and for  
37 improved models of the mechanical behavior of fault slip, including earthquake nucleation and slip  
38 rates (Nelson, 1985; Tinti et al., 2005; Maerten and Maerten, 2006; Jenkins et al., 2009; Perrin et  
39 al., 2016).

40 Results from many studies on fault damage zones are available in the literature. In  
41 particular, some of them investigated the geometry and architecture of different types of damage  
42 zones (McGrath and Davison, 1995; Kim et al., 2004; Choi et al., 2016; Peacock et al., 2017), and  
43 also their scaling properties (Cowie and Scholz, 1992; Knott et al., 1996; Schlische et al., 1996;  
44 Faulkner et al., 2011; Torabi and Berg, 2011). Other studies focused on fault displacement gradient  
45 variability (Cartwright et al., 2002; Shipton and Cowie, 2003; Nixon et al., 2014), the growth  
46 modalities of fault and damage zones (Childs et al., 1996; Cowie and Shipton, 1998; Vermilye and  
47 Scholz, 1998; Gupta and Scholz, 2000; Walsh et al., 2003; Soliva and Benedicto, 2005; de  
48 Joussineau and Aydin, 2007), the intensity and spatial arrangement of associated fractures and the  
49 lithological properties modifications (Berg and Skar, 2005; Micarelli et al., 2003; Savage and  
50 Brodsky, 2011; Balsamo et al., 2019; Torabi et al., 2019). Nevertheless, quantification of mutual  
51 relationships between fractures in damage zones, i.e. connectivity, has been studied by few authors  
52 (Micarelli et al., 2006; Nixon et al., 2011, 2012; Morley and Nixon, 2016; Duffy et al., 2017;  
53 Procter and Sanderson 2018). Recent work highlighted the effectiveness of topological analysis in  
54 the assessment of fracture network connectivity and also quantification of frequency and intensity  
55 (Sanderson and Nixon, 2015, 2018).

56 In this contribution, we present the results of the study of fracture network attributes across  
57 the footwall damage zone of the Compione Fault, an extensional fault zone in the Northern  
58 Apennines, which accumulated about 1.5 km offset in the study area since Early Pliocene times  
59 (e.g. Lucca et al., 2018). We applied the window sampling method (Mauldon et al., 1998;  
60 Sanderson and Nixon, 2015) to cross-sectional exposures of thick sandstone strata, moving away  
61 from the fault core along a structural transect perpendicular to the fault zone strike, to characterize  
62 the spatial arrangement of fracture orientation, intensity, frequency, topology and connectivity.  
63 Implications on fracture attribute variability on the evolution of regional-scale damage zones and  
64 fluid flow patterns are discussed.

65

## 66    **2. Geological framework**

67            The Compione Fault belongs to the northeastern basin-boundary fault system of the  
68 Northern Lunigiana Basin, in the Northern Apennines (Fig. 1A). The basin developed in the  
69 hanging wall of a major NE-verging out-of-sequence thrust in the Northern Apennines, bringing the  
70 Adria passive margin Tuscan Succession onto the allochthonous, ocean-derived Ligurian Succession  
71 in Tortonian times (Fig. 1B; Boccaletti et al., 1971; Elter and Pertusati, 1973; Elter, 1975; Vescovi  
72 et al., 2005; Molli et al., 2018). Such an out-of-sequence thrusting episode overprinted initial in  
73 sequence thrusting of the Ligurian Succession onto the Tuscan one (e.g. Elter and Schwab, 1959;  
74 Principi and Treves, 1984) and, in turn, was followed by synorogenic extension, recorded by  
75 exhumed low-angle detachments crosscut by high-angle extensional fault systems (Carmignani and  
76 Kligfield, 1990; Storti, 1995; Decandia et al., 1998; Jolivet et al., 1998; Clemenzi et al., 2014; Molli  
77 et al., 2018). This Cenozoic polyphasic tectonic pathway affected the Apennines orogenic belt as a  
78 consequence of both the complex evolution of the plate boundary setting between Adria and Europa  
79 plates, and the internal dynamics of the growing thrust wedge (Malinverno and Ryan, 1986;  
80 Royden, 1988; Dewey et al., 1989; Doglioni, 1991; Molli et al., 2018). In such a long lasting  
81 evolution, Plio-Quaternary extension in the Lunigiana Basin, as well as in the other basins  
82 developed along the Tyrrhenian Sea side of the Apenninic belt, has been classically associated with  
83 the eastward propagation of crustal thinning in the back-arc basin, overprinting orogenic contraction  
84 (Elter et al., 1975; Carmignani et al., 1995; Barchi et al., 1998; Jolivet et al., 1998; Martini et al.,  
85 2001).

86            In more detail, the Northern Lunigiana Basin developed since Early Pliocene times in its SE  
87 part, and since Early Pliostocene times in its NW area (Azzaroli, 1977; Federici, 1978; Raggi, 1985,  
88 Boccaletti et al., 1992). It is bounded to the NE by the NW-SE striking, SW dipping Northern  
89 Lunigiana Extensional Fault System, which is longer than 30 km and juxtaposes the Upper  
90 Cretaceous Ottone Flysch of the Ligurian Succession in the hanging wall, against the Chattian to  
91 Aquitanian Macigno Formation sandstones in the footwall, (Fig. 1A; Elter et al., 1975; Bernini and  
92 Lasagna, 1988). The about 15 km long Compione Fault is a major segment of the Northern  
93 Lunigiana Extensional Fault System (Fig. 1A) and penetrates into the metamorphic basement at 6 to  
94 7 km depth (Camurri et al., 2001; Argnani et al., 2003; Lucca et al., 2018), accumulating more than  
95 1.5 km of maximum extensional displacement (Fig. 1B; Bernini and Lasagna, 1998).

96

## 97    **3. Methodology**

98 We studied fracture network attribute distribution along a structural transect in the footwall  
 99 of the Compione Fault, oriented perpendicularly to the fault strike (Fig. 2A). Thirty-five circular  
 100 scan windows (Mauldon, 1998) located on SSW-NNE (between N20°-N60°) striking vertical  
 101 exposures of thick Macigno Fm. sandstone strata, were performed at increasing distance between 80  
 102 and 1030 meters from the Compione fault core, to analyze fracture apparent dip, frequency,  
 103 intensity and connectivity in the footwall damage zone. Deterioration of outcrop quality and  
 104 increasing debris cover prevented data collection closer to the fault core (Fig. 2B). A scan window  
 105 diameter of 0.5 m was selected as the best compromise between the size of clean exposures and the  
 106 need of including at least 30 nodes per window (Fig. 3A; Mauldon, 1998). After checking the 3D-  
 107 orientations of fractures and outcrop surfaces (Fig. 3B), scan windows were performed on  
 108 photographs acquired with a Sony Alpha 6500 camera, equipped with a Sony Sonnar FE 55 mm  
 109 lens. To minimize any possible distortion, the camera was mounted on a tripod and the lens was  
 110 oriented perpendicularly to the outcrop surface (Fig. 3A). The FracPaQ2D tool for MATLAB  
 111 (Healy et al., 2017) was used to extract area-weighted fracture dip directions and total fracture  
 112 lengths from digitized fracture maps (Fig. 3C). Fracture dip data were plotted on half-rose diagrams  
 113 in SSW-NNE oriented vertical planes. Early conjugate and late fracture dips were plotted separately  
 114 (Fig. 2C).

115 Topology concerns relations between different elements of a system, which are scale and  
 116 geometry invariant. In fracture systems, these relations are represented by intersection points  
 117 between fractures, i.e. nodes, and by the segments connecting them, i.e. branches. Fracture network  
 118 topology and connectivity were quantified following the node and branch counting approach of  
 119 Sanderson and Nixon (2015). Nodes are subdivided in three types, according to Manzocchi (2002),  
 120 namely isolated tips (I nodes), splays and abutments (Y nodes) and crossing fractures (X nodes; Fig.  
 121 3C). Branches are also divided in three types: isolated (I-I), partially connected (I-C) and fully  
 122 connected (C-C). Number of nodes ( $N_I$ ,  $N_Y$ ,  $N_X$ ), circular window areas ( $\pi r^2$ ), and total fracture  
 123 length ( $\Sigma L$ ) were used to calculate the following parameters (Procter and Sanderson, 2018):

124	(1) Number of fractures	$N_L = (N_I + N_Y)/2$	
125	(2) Number of branches	$N_B = (N_I + 3N_Y + 4N_X)/2$	
126	(3) Areal fracture frequency	$P_{20} = N_L/\pi r^2$	(m <sup>-2</sup> )
127	(4) Areal branch frequency	$B_{20} = N_B/\pi r^2$	(m <sup>-2</sup> )
128	(5) Areal fracture intensity	$P_{21} = \Sigma L/\pi r^2$	(m <sup>-1</sup> )
129	(6) Dimensionless fracture intensity	$P_{22} = (\Sigma L)^2 / N_L * \pi r^2$	
130	(7) Dimensionless branch intensity	$B_{22} = (\Sigma L)^2 / N_B * \pi r^2$	

131 For comparison, areal fracture intensity was also calculated by counting the number of fracture  
132 intersections  $N_E$  (edge-nodes) with the circular window circumference (Mauldon, 1998):

133 (8) 1-D fracture intensity  $P_{10} = N_E/4r$  (m<sup>-1</sup>)

134 Since  $P_{21}$  is dependent only on fracture length, fracture intensity values of late fractures are  
135 calculated separately from early conjugate fractures orthogonal to bedding.  $P_{22}$  and  $B_{22}$  have been  
136 shown to be the most suited parameters to define when a fracture network forms a spanning cluster  
137 and, therefore, overcomes the percolation threshold (defined by a specific critical values of  $P_{22C}$  and  
138  $B_{22C}$ ) in a two-dimensional system (Robinson, 1983, 1984; Balberg et al., 1984; Sanderson and  
139 Nixon, 2018).

140

## 141 4. Results

### 142 4.1. Damage zone architecture

143 Away from the fault zone, Macigno Fm. sandstone strata dip 5°-10° towards the NE (Figs.  
144 2A, B) and the fracture network includes a fracture set nearly perpendicular to bedding and another  
145 one parallel to primary depositional structures, likely produced by de-compaction during  
146 exhumation. Approaching the fault core, bedding is progressively tilted towards the SSW and  
147 acquires dip values up to about 60° at the damage zone-fault core transition (Figs. 2A, B). Within  
148 the fault zone, Macigno Fm. thick sandstone strata are affected by abundant Prehnite-Quartz-Calcite  
149 conjugate shear fracture arrays striking parallel to the Compione Fault trend and having acute  
150 bisectors generally orthogonal to bedding, regardless of bedding dip (Fig. 2B; Lucca et al., 2018).  
151 Shear fractures commonly underwent different degrees of cementation, dissolution, re-opening and  
152 shearing. Cumulative orientation data analysis shows fracture dip values between 10° and 50° to the  
153 NNE, which restore to values between 60° and 90° to the NNE when bedding is rotated to the  
154 horizontal (Figs. 2C, D). A major E-W striking, S dipping fault splay of the Compione Fault  
155 intersects the structural transect at a distance of about 300 m away from the fault core (Figs. 2A, B).  
156 Fracture network patterns in different structural sectors are shown in Figs. 2E, F, G. In the inner  
157 sector of the footwall damage zone, late subsidiary fault zones developed after fault-related folding  
158 and Macigno Fm. sandstone strata were exploited as slip surfaces (Fig. 2C). These fault zones dip  
159 60-80° to both the SSW and NNE.

160

### 161 4.2. Fracture orientations

162 More than ten thousand (10,479) fracture dip measurements were extracted from the  
163 digitized fracture maps (Fig. 4). Qualitative analysis of fracture patterns clearly illustrates an overall  
164 decreasing fracture frequency and variable orientations moving away from the fault core, despite a  
165 regular trend cannot be identified. Late fractures occur from W1 up to W20.

166 Fracture dips cumulated by structural sector are represented in Figure 5A. Moving away the  
167 fault core, it is evident how early conjugate fractures are progressively characterized by higher dip  
168 values. The majority of early fractures dip  $10^{\circ}$ - $30^{\circ}$  to the NNE in the innermost structural sectors,  
169 where bedding dips  $50^{\circ}$ - $60^{\circ}$  and  $45^{\circ}$  to the SSW for sector 1 and 2, respectively. Sectors 3 and 4,  
170 which have bed dips comprised between  $35^{\circ}$ - $45^{\circ}$ SSW and  $10^{\circ}$ - $20^{\circ}$ SSW, respectively, are  
171 characterized by early fractures mostly dipping  $30^{\circ}$ - $50^{\circ}$  to the NNE. In sector 4, subvertical early  
172 fractures also occur. The outermost structural sectors (5 and 6), where bedding ranges from  
173 horizontal to  $10^{\circ}$  dipping to the NNE, show early fracture dips  $>60^{\circ}$  up to subvertical. Late fractures  
174 crosscutting early ones occur abundantly in sector 1, up to sector 3 where they mostly re-activate  
175 the latter. Late fractures are characterized by Andersonian to subvertical dip values, i.e.  $60^{\circ}$ - $80^{\circ}$ ,  
176 independently from bedding orientation (Fig. 5A). Figure 5B shows dip values of early fractures  
177 after restoring bedding to the horizontal in sectors 1 to 5. We observe that early conjugate fracture  
178 dips are still slightly inclined to the NNE in all the restored sectors, apart from sector 1. Dip values  
179 better fit an Andersonian extensional stress field with an additional  $10^{\circ}$  clockwise-rotation (Fig.  
180 5C).

181 In more detail, in structural sector 1, W1 is characterized by early fractures dipping  $40^{\circ}$ - $60^{\circ}$  to the  
182 NNE and late fractures dipping  $70^{\circ}$ - $90^{\circ}$  to the SSW. W1 is the only scan window in which late  
183 fractures are pervasively developed. Late fractures acquire dip values of about  $60^{\circ}$  in W4, and even  
184 lower values in W5 and W8. W6 and W9 are characterized by early fractures only, showing dip  
185 values ranging from  $20^{\circ}$  to  $80^{\circ}$  to the NNE. Conversely, in window W7, fractures mostly dip  $20^{\circ}$  to  
186  $30^{\circ}$  towards the SSW (Fig. 6). In structural sector 2, dip values of fracture in W13 are more  
187 scattered, varying from  $10^{\circ}$  to  $50^{\circ}$  towards NNE and from  $20^{\circ}$  to  $70^{\circ}$  in W12. Late fractures in W14  
188 show lower dip values, between  $20^{\circ}$  and  $60^{\circ}$ . In structural sector 3, windows W15 to W18 show  
189 early fractures mostly dipping from  $10^{\circ}$  to  $60^{\circ}$  towards the NNE. W19 has early fractures with dip  
190 values between  $50^{\circ}$  and  $90^{\circ}$  and W20 is characterized by more scattered values displaying two  
191 maxima, at  $40^{\circ}$ - $50^{\circ}$  and  $80^{\circ}$ - $90^{\circ}$  to the NNE. Few late fractures occur in this structural sector and  
192 show scattered dip values (Fig. 6). In structural sector 4, early fractures dip values are more variable  
193 than in the previous sites. In particular, at W21 the most frequent dip values occur between  $30^{\circ}$  to  
194  $50^{\circ}$  towards NNE; at W22 it slightly shallows to  $20^{\circ}$  to  $40^{\circ}$ . Windows W23 and W25 are  
195 characterized by mostly near vertical fractures, whereas at site W24 fractures dip mostly  $50^{\circ}$  to  $70^{\circ}$

196 towards the NNE (Fig. 6). In structural sector 5, W26 shows fracture dip values clustered in two  
197 maxima, between 30° and 70° to the NNE, and 60° to 80° to the SSW, respectively. Windows W27  
198 and W29 are characterized by fracture dip values spanning between 50° and 90° to the NNE,  
199 whereas fractures are near vertical, from 80° SSW to 80° NNE, at site W28. In structural sector 6,  
200 most fractures are sub-vertical to 60° dipping. Conversely, sites W33 and W35 are characterized by  
201 fracture dip maxima at 60° to 70° to the SSW and 20° to 30° to the NNE, respectively (Fig. 6).

202 Summarizing, the highest early fractures dip values frequency is mostly at high angle to  
203 bedding in each structural sector. Late fractures, conversely, occur in sectors 1, 2 and 3 and their dip  
204 values are mostly >60° to subvertical both to the SSW and NNE, irrespectively of bedding dip.

205

#### 206 4.3. Fracture intensity, frequency and dimensionless intensity distributions

207 Plotting  $P_{21}$  values grouped by structural sector vs. distance from the fault core allows to  
208 appreciate the decreasing trend of fracture intensity in the damage zone (Fig. 7A). Mean values of  
209  $P_{21}$  and  $P_{10}$  per structural sector are reported in Table 1, while the whole dataset is in Table S1.  
210 Sector 1 shows the highest fracture intensity with a  $P_{21}$  value of  $54.8 \pm 13.6 \text{ m}^{-1}$  and a  $P_{10}$  value of  
211  $44.9 \pm 9.7 \text{ m}^{-1}$ , which well agrees with the value of  $P_{21}$  calculated for early fractures only,  
212 corresponding to  $45.5 \pm 13.3 \text{ m}^{-1}$ . Structural sectors 5 and 6 are characterized by the lowest  $P_{21}$   
213 values, corresponding to  $23.2 \pm 8 \text{ m}^{-1}$  and  $25.1 \pm 11.5 \text{ m}^{-1}$ , respectively, and  $P_{10}$  values of  $23.0 \pm 9.1$   
214  $\text{m}^{-1}$  and  $21.3 \pm 8.2 \text{ m}^{-1}$ , respectively. Overall,  $P_{21}$  and  $P_{10}$  values are quite comparable for structural  
215 sectors 4, 5 and 6. Approaching the fault core,  $P_{10}$  systematically provides lower values than  $P_{21}$ ,  
216 which fairly correspond to  $P_{21}$  calculated taking into account early fractures only (Fig. 7A).

217  $P_{21}$  values in scan windows range from  $71.9 \text{ m}^{-1}$  in W3 to  $15.9 \text{ m}^{-1}$  in W28, with an outlier of  $3.1 \text{ m}^{-1}$   
218 at W33. Analogously,  $P_{10}$  values range from  $58 \text{ m}^{-1}$  at W3 to  $12 \text{ m}^{-1}$  at W28, with W33 showing  $6$   
219  $\text{m}^{-1}$  (Fig. 7B). Overall,  $P_{21}$  decreases with increasing distance from the Compione fault core.  $P_{21}$   
220 values are best fit by a lognormal probability distribution function, whereas  $P_{10}$  values are best fit  
221 by a linear one. In both cases, scattering is quite high.  $P_{21}$  has been calculated also for early  
222 conjugate fractures only, in structural sectors 1 to 3, where late fractures also occur. Early fractures  
223  $P_{21}$  still shows a decreasing trend with increasing distance from the fault core and is fitted by a  
224 linear function, which is similar to the one fitting  $P_{10}$ .

225 Fracture ( $P_{20}$ ) and branch ( $B_{20}$ ) frequencies grouped by structural sectors vs. distance from  
226 the fault core show different trends compared to fracture intensity (Table 1; Fig. 7C). In particular,  
227 sectors 1 to 3 are characterized by similar values, i.e.  $287 < P_{20} < 330 \text{ m}^{-2}$  and  $1322 < B_{20} < 1528 \text{ m}^{-2}$ .

Then, between sectors 3 and 4, an abrupt drop of frequencies is evident, which show ranges of 139 to 207 m<sup>-2</sup> and of 567 to 594 m<sup>-2</sup> for P<sub>20</sub> and B<sub>20</sub>, respectively. The largest standard deviations occur in sectors 1 and 3, due to outliers. P<sub>20</sub> values in scan windows span from 479 m<sup>-2</sup> in W1 to 71 m<sup>-2</sup> in W28, excluding the highest and lowest values, of 576 m<sup>-2</sup> and of 10 m<sup>-2</sup> in W16 and W33, respectively (Fig. 7D). Similarly, the lowermost values of B<sub>20</sub> are 204 m<sup>-2</sup> in W28 and 51 m<sup>-2</sup> in W33. Highest branch frequencies are in W3, W1 and W20 and show values of 2353, 2277, and 2165 m<sup>-2</sup>, respectively. Fracture frequency P<sub>20</sub> values are poorly fitted by a lognormal probability distribution function and branch frequency B<sub>20</sub> is fitted by a linear function, both showing extremely low coefficients of determination (Fig. 7D). Dimensionless fracture and branch intensity parameters P<sub>22</sub> and B<sub>22</sub> also show clear decreasing trends moving away from the fault core. P<sub>22</sub> mean values vary from 9.70 ± 1.81 in sector 1 to 3.02 ± 1.84 in sector 6 (Fig. 7E). P<sub>22</sub> values in scan windows range from 13.78 in W4 to 0.97 in W33 and are best fit by an exponential probability distribution function although data are also fit by linear and lognormal functions having similar coefficients of determination (Fig. 7F). B<sub>22</sub> mean values span from a maximum of 1.96 ± 0.18 in sector 1 to a minimum of 0.95 ± 0.44 in sector 5 (Table 1; Fig. 7G). Sector 6 has a B<sub>22</sub> of 1.06 ± 0.59 due to higher values in W30 and W32. B<sub>22</sub> values in scan windows are best fit by a lognormal probability distribution function and range between 2.38 in W4 and 0.19 in W33 (Fig. 7H).

245

#### 246 4.4. Fracture network topology

247 Network topology can be classified by the relative proportions of I, X, and Y nodes and I-I,  
 248 I-C and C-C branches in both structural sectors and in each scan window (Fig. 8; Table 1). In the  
 249 ternary I, Y, X plot, structural sectors mean relative proportions follow the curved path highlighted  
 250 in Figure 8A. The relative abundance of I nodes is 0% at site W8 and then typically remains lower  
 251 than 20% in structural sectors 1 to 4 (scan windows W1 to W26). It increases to 20-25% in sector 5  
 252 (sites W27 to W29) and, eventually, up to about 52% in scan window W35. The relative abundance  
 253 of X nodes varies from 20 to 40% in structural sectors 1 to 4 and then lowers down to about 7 to  
 254 17% in sectors 5 and 6. Scan windows W26 and W33 make exception to this trend and show  
 255 percentages higher than 40%. The relative abundance of Y nodes does not show a systematic trend  
 256 with structural sectors. Relative proportions typically vary between 40 and 70 %, in most scan  
 257 windows, with higher values at sites W8, W21 and W28, and lower ones at W33 and W35 (Fig.  
 258 8A). In the branch types ternary diagram, whose lower right corner is represented in Figure 8B,  
 259 relative proportions of all scan windows are clustered towards the C-C vertex. An exception is  
 260 provided by scan windows belonging to structural sector 6, which are characterized by relative



261 proportions of C-C branches of 70 to 80%, and even as low as 58% in W35, most of the remaining  
262 windows have  $C-C > 90\%$  (Fig. 8B).

263 Parameters  $C_L$  and  $C_B$  indicate the number of connections per fracture and per branch,  
264 respectively, and are derived from network topology.  $C_L$  and  $C_B$  values grouped by structural sector  
265 show decreasing connectivity moving away the fault core (Table 1). Specifically,  $C_L$  values span  
266 from a maximum of 5.76 in sector 1 to 3.02 in sector 6.  $C_B$  values are above 1.92 in sectors 1 to 4,  
267 approaching maximum connectivity per branch (equal to 2), and drops to 1.71 in the outermost  
268 sector.  $C_B$  in scan windows decreases below a value of 1.80 in windows belonging to sector 6 and  
269 shows a value of 1.49 in W35.

270 The total number of nodes per scan window shows quite a large variability when plotted  
271 versus the distance from the Compione fault core (Fig. 9A). Maximum values of 280 occur at sites  
272 W1 and W3, while values lower than 100 were obtained at distances higher than about 600 m from  
273 the fault core. Overall, a decreasing trend with decreasing bedding dip can be envisaged and  
274 described by a quite poor linear best fit. I nodes are mostly lower than 30 per scan window and do  
275 not show any trend with increasing distance from the fault core (Fig. 9B). Conversely, such a trend  
276 occurs for X nodes, which are more than 60 per window in structural sector 1 and decrease down to  
277 less than 20 per scan window from W27 to W35 (Fig. 9C). The number of Y nodes also decreases  
278 with distance from the fault core, from 171 at site W1, down to less than 60 from W21 to W35. Y  
279 nodes vary to a higher degree and, consequently, a quite poor linear best fit was obtained (Fig. 9D).  
280 The number of total nodes per circular window shows a quite good positive correlation with the  
281 corresponding fracture intensity values  $P_{21}$  (Fig. 10A). The same cannot be said when only I nodes  
282 are analyzed because a trend cannot be identified (Fig. 10B). On the other hand, good positive  
283 linear correlations occur for X and Y nodes plotted versus  $P_{21}$  values (Figs. 10C, D).

284

## 285 5. Discussion

286 Results from this study indicate that window sampling techniques, which were typically  
287 designed for quantifying fracture attributes in map view (e.g. Mauldon, 1998; Sanderson and Nixon,  
288 2015), can be effectively applied to cross-sectional exposures of thick to very thick strata, i.e.  
289 within single mechanical layers. A typical limitation of studies in map view is that collection of 2D  
290 datasets in thick strata is expected to imply a significant uncertainty when trying to build 3D  
291 discrete fracture networks because of the lack of reliable information on the third dimension. In our  
292 case, unavailability of suitable exposures in map view prevented any attempt to combine 2D

293 datasets in mutually orthogonal surfaces and produce a 3D discrete fracture network geometry.  
294 Accordingly, we rely on 2D vertical exposures to speculate on spatial variations of fracture  
295 attributes and network topology, and their implications on fluid flow and fault damage zone  
296 evolution.

297

## 298 5.1 Fracture attributes spatial trends

299 Fracture intensity values in the damage zone are characterized by an increasing trend  
300 approaching the fault core (Figs. 11A). It is interesting to note that  $P_{10}$  are always lower than  $P_{21}$   
301 values. Such a difference is the result of the faster increase of total fracture length inside scan  
302 windows compared to the number of fracture intersections with scan circumferences, i.e.  $N_B/N_L$   
303 increases. Fracture intensities in structural sectors 1 to 3 are comparable to 1-D fracture frequencies  
304 (expressed in  $m^{-1}$  as  $P_{21}$ ) reported from many inner damage zones of extensional and strike-slip fault  
305 zones, while intensities from the outermost sectors are slightly higher than those measured in outer  
306 damage zones (e.g. Knott et al., 1996; Berg and Skar, 2005; Choi et al., 2016; Balsamo et al., 2019;  
307 Torabi et al., 2019). Nevertheless, microfracture frequencies are significantly higher than meso- to  
308 macroscale fractures (de Joussineau et al., 2007; Faulkner et al., 2011; Savage and Brodsky, 2011)  
309 due to their cumulative length frequencies, which are fit by power law distributions (Hudson and  
310 Priest, 1979; Pickering et al., 1995; Odling et al., 1999; Zeeb et al., 2013). Therefore, regardless  
311 from absolute values, which depend on scan window size and resolution, our results show that  
312 fracture attributes have a remarkably low rate of decay moving away from the fault core. In fact,  
313 they retain fracture intensities typical of outer damage zones up to 900 m from the fault core, at  
314 least in the measured mechanical layers, i.e. plurimetric thick turbiditic sandstone strata (Fig. 11A).  
315 This width is out of scale with published displacement-damage zone width relationships (Cowie and  
316 Scholz, 1992; Schlische et al., 1996, Shipton and Cowie, 2003; Savage and Brodsky, 2011; Torabi  
317 and Berg, 2011).

318 On the other hand, the spatial distribution of late fractures occurring from sectors 1 to 3 and  
319 associated with subsidiary fault zones at high-angle irrespectively of bedding orientation, would be  
320 coherent with observed scaling relationships if we assume that the inner part of the studied transect  
321 is located in the linking damage zone (*sensu* Kim et al., 2004) defined by the Compione Fault and  
322 its major E-W footwall splay fault (Figs. 2 and 6B). Inner structural sectors, which are interested by  
323 late fractures, show significantly higher  $B_{20}$  and  $P_{20}$  values compared to outer sectors (4 to 6).  
324 Specifically,  $B_{20}$  has an almost threefold increase, which is reasonably caused by the superposition  
325 of early rotated and late high-angle conjugate fracture sets (Fig. 11A). Late fractures are only

pervasively developed in scan window W1 and completely overprint the rotated conjugate shear fracture pattern causing intense outcrop degradation moving towards the Compione fault core. Speculating on the complex architecture of the studied transect, we propose that this intensely degraded sector constitutes the inner damage zone of the Compione Fault, which accommodated deformation even after slip localization (Lucca et al., 2018).

Overall, high fracture intensity and density values reported in this study, which were collected from single mechanical layers, reasonably result from the sum of the contributions of a hierarchical distribution of subsidiary fault zones (Ackermann and Schlische, 1997; Bour and Davy, 1999) in the damaged rock volume of the structurally complex Compione extensional fault zone, and are only representative of the mesoscale fracture pattern in very thick sandstone strata, which show a different mechanical behavior when compared with thin strata.

## 5.2 Connectivity of the damage zone fracture network

A 2D fracture network can be above or below the percolation threshold, which is the point above which the network is connected. As the threshold is approached, the size of the largest cluster increases until, at the threshold, it becomes a spanning cluster. Many parameters have been used to quantify the proximity to the percolation threshold, in particular fracture ( $P_{22}$ ) and branch ( $B_{22}$ ) dimensionless intensity, and number of connections per fracture ( $C_L$ ) and per branch ( $C_B$ ). The parameters critical values, i.e. at percolation threshold conditions, have been demonstrated to be influenced by the orientation distribution, intensity, and topology of the network (Robinson, 1983, 1984; Balberg et al., 1984; Manzocchi, 2002; Nixon et al., 2018). These critical values have been calculated from stochastic simulations of different simplified fracture network patterns. We refer to critical  $C_{LC}$  and  $C_{BC}$  values for conjugate fracture systems, i.e.  $60^\circ$  between the two sets. Measured  $C_L$  are above the critical values of 3.11 except for half of the scan windows of sector 6. Even measured  $C_B$  values are always above 1.51 in all scan windows unless W35 (Table S1).

Number of connections, anyway, are only topology dependent. Dimensionless intensity parameters (Fig. 11B), conversely, quantify the connectivity and, therefore, the proximity to the percolation threshold, from intensity and average length measurements. Manzocchi (2002; Figs. 10, 13) and Nixon et al. (2018; Fig. 9B) calculated the critical values of fracture ( $P_{22C}$ ) and branch ( $B_{22C}$ ) dimensionless intensities for any topology. By comparing the calculated critical values with measured values in the studied transect for the appropriate topologies, only structural sector 6 is slightly below the percolation threshold, consistently with  $C_L$  and  $C_B$ .

358       The damage zone of the Compione Fault is characterized by increasing amounts of X and Y  
359 nodes approaching the fault core, and the latter are systematically more abundant (Fig. 11C). This  
360 can be simply explained by noting that small amounts of slip on two conjugate shear fractures  
361 forming a X node, produces two Y nodes. The almost linear increase of X nodes might relate to the  
362 formation of the damage zone, where a positive gradient of conjugate shear fracture abundancy  
363 towards the prospect master slip zone was imprinted in the very early evolutionary stages (Lucca et  
364 al., 2018). The increase of Y nodes at an overall comparable rate might relate to the same  
365 phenomenon, i.e. an increase of displacement associated with shear fracturing. The only deviation  
366 from this behavior occurs in sector 3, where the major E-W splay fault zone occurs and caused  
367 additional shearing, linkage and/or splaying of conjugate arrays (Fig. 11C). The higher number of I  
368 nodes in structural sector 6 compared to the other ones, may indicate that it lies at the outer  
369 boundary of the damage zone, because fault-related fracture networks are typically dominated by Y  
370 nodes (Nixon et al., 2012; Morley and Nixon, 2016; Duffy et al., 2017). This interpretation is  
371 supported by the dominantly bed-perpendicular attitude of fractures and, therefore, the  
372 corresponding lower connectivity (Fig. 6).

373       The studied damage zone, the fracture network is overall characterized by high relative  
374 percentages of connecting nodes compared to previous information reported in the literature.  
375 However, it has to be emphasized that we measured conjugate fracture systems related to a regional  
376 scale fault zone in cross-section, whereas published topological analyses were performed on high-  
377 angle lineaments in map view (Morley and Nixon, 2016; Duffy et al., 2017), distributed strike-slip  
378 faults (Nixon et al., 2012; Procter and Sanderson, 2018) and metric offset extensional faults  
379 (Micarelli et al., 2006). This means that the high connectivity of the studied fracture network in the  
380 vertical and cross-fault directions of a structurally complex fault zone with maximum displacement  
381 approaching 1.5 km, is reasonable and expected.

382

### 383 *5.3 Implications on damage zone evolution*

384       Formation of conjugate shear fracture arrays with acute angle bisectors generally orthogonal  
385 to bedding in the damage zone, may have occurred either before or during bedding rotation. In the  
386 first case, it would have occurred in the tip damage zone stage of the propagating extensional fault,  
387 before folding. Alternatively, conjugate shear fractures would have formed during fault-related drag  
388 folding, implying fracture dip scattering increasing towards the fault core, i.e. increasing with bed  
389 rotation. Fracture dip frequency standard deviation values grouped by structural sectors do not  
390 display any increasing trend approaching the fault core, as it would be expected if conjugate

fractures formed synchronously with folding (Fig. 12). Conversely, the lowest standard deviation value of  $\pm 27^\circ$ , corresponds to structural sector 1, while the highest value of  $\pm 40^\circ$ , to structural sector 4. Therefore, fracture dip frequency distributions suggest conjugate fracture arrays nucleation in an early stage of damage zone development.

Also angular relationships between fracture cross-sectional orientations and bedding (Fig. 5) support early formation of conjugate shear fractures in the tip damage zone (*sensu* Kim et al., 2004) of the blind Compione Fault, before extensional fault-propagation folding and breakthrough in the Macigno Fm. sandstones (Hardy and McClay, 1999; Jin and Groshong, 2006; Lucca et al., 2018). In more detail, assuming that the crest to forelimb transition of the out-of-sequence thrust-related anticline was located between structural sectors 5 and 6, restoration of fracture geometry at the pre fault-related folding stage results in southwestward tilted conjugate vein arrays in sectors 2 to 5, with their bisectors inclined to the NE (Fig. 5B). This is not expected in extension-related deformation, where conjugate fault arrays typically have vertical bisectors representing the orientation of the principal axis of the stress ellipsoid (e.g. Anderson, 1951). A possibility for explaining such a discrepancy relies on the very poor constraints that are available on the pre-extensional, cross-sectional shape of the regional anticline. The conservative solution of locating the crest-to-forelimb hinge area between structural sectors 5 and 6 can be released and the transition from flat-lying to eastward dipping strata can be moved to the southwest, in between structural sectors 1 and 2. This hypothesis implies an additional clockwise (towards NNE) rotation of fracture sets to match bedding attitude from sectors 2 to 5 with that of the forelimb in sector 6. The result of such a rotation is the restoration of conjugate fracture bisectors to a vertical attitude (Fig. 5C). Formation of conjugate shear fracture arrays with vertical bisectors in gently northeastward dipping strata, can mechanically help explaining the higher abundance of northeast-dipping fractures if stress channeling (Mandl, 2000) is assumed to have occurred in thick and strong beds.

Summarizing, formation of the blind Compione extensional fault zone initially caused development of a  $\sim 900$  m wide tip damage zone in the Macigno Fm. thick sandstone beds. The initial fracture pattern was characterized by conjugate fracture arrays with vertical bisectors and fracture intensity increasing almost linearly towards the prospect fault core (Fig. 13A). Propagation of the fault tip induced passive extensional folding of the damage zone and consequent antithetic re-activation of properly oriented, early conjugate fracture arrays whereas other early fractures became misoriented in the extensional stress field. Fault zone evolution progressed by interaction with the E-W footwall splay fault and development of new subsidiary high-angle faults to accommodate further extensional deformation up to about 500 m away from the prospect master slip zone (Fig.

13B). Fault zone interaction favored formation of late-stage high-angle subsidiary fault zones formed and accommodation of additional offset in the linking damage zone (Fig. 13C).

#### *5.4. Implications for fluid flow in extensional fault systems*

Damage zones of extensional fault systems are composed of a superposition of deformation patterns developed during nucleation, propagation, offset accommodation, and also interaction of their fault segments (Kim et al., 2004; Choi et al., 2016; Peacock et al., 2017). The intensity of these deformation structures generally increases logarithmically approaching fault cores (Berg and Skar, 2005; Savage and Brodsky, 2011; Torabi et al., 2019). High angle dilational and shear fractures, and subsidiary faults in cohesive rocks can represent effective conduits for fluid flow (Caine et al., 1996; Faulkner et al., 2010). In this the very thick sandstone strata involved in the Compione footwall damage zone case, the dense network of connected early, conjugate shear fractures with vertical bisectors significantly increased secondary porosity and permeability, providing efficient vertical conduits to vertical fluid flow, as proved by formation of a hydrothermal plume in the fault process zone, which was likely sealed by the overlying clay-rich Ottone Flysch (Lucca et al., 2018). At this stage, in the hydromechanical stratigraphy of the Compione Fault footwall, fractured thick sandstone strata would have provided an efficient reservoir for fluid accumulation and along-strike migration. Further fault zone evolution, characterized by fault propagation, linkage, additional fracturing, and bed rotation, caused a further increase of the hydraulic connectivity, likely breaching the previously formed reservoir and favoring fluid migration.

## **6. Conclusions**

The Compione Fault is a segment of the Northern Lunigiana, regional-scale extensional fault system, affecting the Tyrrhenian Sea side of the Northern Apennines orogenic wedge since early Pliocene times. The maximum displacement accumulated by the Compione Fault exceeds 1.5 km. In the footwall, the fault zone exposes thick to very thick sandstone strata, where we acquired circular scan windows on vertical outcrops along a transect oriented perpendicular to the fault strike, to quantify fracture network attributes. Our results can be summarized by the following main points:

- fracture attributes in this regional-scale damage zone have classic logarithmic and linear decreasing trends moving away from the fault core, but with a low rate of decay in the investigated mechanical layers;

- $P_{21}$  and  $P_{10}$  values are similar in the outer tip damage zone whereas, approaching the fault core, the latter parameter systematically underestimates fracture intensity in more intensely deformed sectors, where the branch-to-fracture ratio increases;
- fracture connectivity is higher than the percolation threshold value in all structural sectors within the tip damage zone and this indicates efficient fault-controlled fluid circulation since the very early evolutionary stages;
- fault-related fracturing evolved from initial formation of ~ 900 m wide footwall tip damage zone ahead of the upward propagating blind fault, which was overprinted later on by a ~ 500 m wide linking damage zone;
- topological analysis supports this interpretation by showing a progressive and almost linear increase of X and Y nodes towards the fault core, being the former mostly imprinted from the onset of the tip damage zone formation;
- restoration of fracture dip in the tip damage zone indicates that the hinge zone of the extensional fault-propagation fold associated with the Compione Fault located about 0.6 km into the forelimb of the out-of-sequence thrust-related anticline, whereas the fault core located close to the crest-to-forelimb transition of the anticline.

## 7. Acknowledgements

We thank C.W. Nixon and D.J. Sanderson for the fruitful suggestions which allowed us to improve the manuscript. We are grateful to F. Balsamo for fruitful discussions on the structure and evolution of the Compione Fault. Author's contribution: A. Lucca carried out field work, collected and analyzed data, and wrote the manuscript; F. Storti conceived the research, participated to some field work, and critically reviewed the manuscript; G. Molli participated to some field work and critically reviewed the manuscript. The corresponding author will provide the full dataset on request.

## References

- Ackermann, R.V., and Schlische, R.W., 1997. Anticlustering of small normal faults around larger faults. *Geology*, vol. 25(12), p. 1127-1130.
- Anderson, E.M., 1951. *The Dynamics of Faulting and Dyke Formation with Application to Britain* (2nd edn). Oliver and Boyd, Edinburgh.

487 Argnani, A., 2002. The Northern Apennines and the kinematics of Europe-Africa convergence:  
 488 Bollettino della Società Geologica Italiana. vol. 1, p. 47–60.

489 Azzaroli, A., 1977. The Villafranchian stage in Italy and the Plio-Pleistocene boundary. *Giornale di*  
 490 *Geologia*, v. 41, p. 61-79.

491 Balberg, I., Anderson, C.H., Alexander, S., and Wagner, N., 1984. Excluded volume and its relation  
 492 to the onset of percolation. *Phys. Rev.*, 30 (7), p. 3933-3943.

493 Balsamo, F., Clemenzi, L., Storti, F., Solum, J., and Taberner, C., 2019. Tectonic control on vein  
 494 attributes and deformation intensity in fault damage zones affecting Natih platform carbonates,  
 495 Jabal Qusaybah, North Oman. *Journal of Structural Geology*, vol. 122, p. 38-57.

496 Barchi, M.R., Minelli, G., and Pialli, G., 1998. The CROP 03 Profile: A synthesis of results on deep  
 497 structures of the Northern Apennines. *Memorie della Società Geologica Italiana*, vol. 52, p. 383–  
 498 400.

499 Berg, S.S., and Skar, T., 2005. Controls on damage zone asymmetry of a normal fault zone: outcrop  
 500 analyses of a segment of the Moab fault, SE Utah. *Journal of Structural Geology*, vol. 27 (10), p.  
 501 1803-1822.

502 Bernini, M., and Lasagna, S., 1988. Rilevamento geologico e analisi strutturale del bacino dell’Alta  
 503 Val Magra tra M. Orsaro e Pontremoli (Appennino Settentrionale): *Atti della Società Toscana di*  
 504 *Scienze Naturali, Memorie, Serie A*, 95, p. 139-183.

505 Bernini, M., Vescovi, P., and Zanzucchi, G., 1997, Schema strutturale dell’Appennino Nord-  
 506 Occidentale: *L’Ateneo Parmense Acta Naturalia*, v. 33, p. 43-54.

507 Boccaletti, M., Elter, P., and Guazzone, G., 1971. Plate Tectonic Models for the Development of the  
 508 Western Alps and Northern Apennines. *Nature*, vol. 234, p. 108-111.

509 Boccaletti, M., Corti, G., and Martelli, L., 2011. Recent and active tectonics of the external zone of  
 510 the Northern Apennines (Italy). *Int. J. Earth Sci.*, vol. 100, p. 1331-1348.

511 Bour, O., and Davy, P., 1999. Clustering and size distributions of fault patterns: theory and  
 512 measurements. *Geophysical Research Letters*, vol. 26(13), p. 2001-2004.

513 Caine, J.S., Evans, J.P., and Forster, J.B., 1996. Fault zone architecture and permeability structure.  
 514 *Geology*, vol. 24, p. 1025-1028.



515 Camurri, F., Argnani, A., Bernini, M., Papani, G., Rogledi, S., and Torelli, L., 2001. The basement  
516 of the NW Apennines: interpretation of reflection seismics and geodynamic implications. Final  
517 Proceedings, Geoitalia 2001, 3° Forum Italiano di Scienze della Terra (Fist), Chieti, Italy, p. 50-51.

518 Carmignani, L., and Kligfield, R., 1990. Crustal extension in the Northern Apennines: The  
519 transition from compression to extension in the Alpi Apuane core complex. *Tectonics*, vol. 9, p.  
520 1275–1303.

521 Carmignani, L., Decandia, F.A., Disperati, L., Fantozzi, P.L., Lazzarotto, A., Liotta, D., and  
522 Oggiano, G., 1995. Relationships between the Tertiary structural evolution of the Sardinia-Corsica-  
523 Provençal Domain and the Northern Apennines. *Terra Nova*, vol. 7, no. 2, p. 128–137.

524 Cartwright, J.A., and Mansfield, C.S., 1998. Lateral displacement variation and lateral tip geometry  
525 of normal faults in the Canyonlands National Park, Utah. *Journal of Structural Geology*, vol. 20, p.  
526 3-19.

527 Chester, F.M., Evans, J.P., and Biegel, R.L., 1993. Internal structure and weakening mechanisms of  
528 the San Andreas fault. *Journal of Geophysical Research*, vol. 98, p. 771-786.

529 Childs, C., Nicol, A., Walsh, J.J., and Watterson, J., 1996. Growth of vertically segmented normal  
530 faults. *Journal of Structural Geology*, vol. 18, p. 1389-1397.

531 Choi, J.H., Edwards, P., Ko, K., and Kim, Y.S., 2016. Definition and classification of fault damage  
532 zones: a review and a new methodological approach. *Earth-Science Reviews*, vol. 152, p. 70-87.

533 Clemenzi, L., Molli, G., Storti, F., Muchez, P., Swennen, R., and Torelli, L., 2014. Extensional  
534 deformation structures within a convergent orogen: The Val di Lima low-angle normal fault system  
535 (Northern Apennines, Italy). *Journal of Structural Geology*, vol. 66, p. 205-222.

536 Cowie, P.A., and Scholz, C.H., 1992. Physical explanation for the displacement-length relation-ship  
537 of faults, using a post-yield fracture mechanics model. *Journal of Structural Geology*, vol. 14, p.  
538 1133-1148.

539 Cowie, P.A., and Shipton, Z.K., 1998. Fault tip displacement gradients and process zone  
540 dimensions. *Journal of Structural Geology*, vol. 20, p. 983-997.

541 de Joussineau, G., and Aydin, A., 2007. The evolution of the damage zone with fault growth in  
542 sandstone and its multiscale characteristics. *Journal of Geophysical Research*, vol. 112,  
543 doi:10.1029/2006JB004711.

544 Decandia, F.A., Lazzarotto, A., and Liotta, D., 1998. The CROP 03 traverse: insights on post-  
545 collisional evolution of Northern Apennines. *Memorie della Società Geologica Italiana*, vol. 52, p.  
546 427–440.

547 Dewey, J.F., Helman, M.L., Knott, S.D., Turco, E., and Hutton, D.H.W., 1989. Kinematics of the  
548 western Mediterranean, In: Coward M.P., Dietrich D., and Park R.G., eds., *Alpine Tectonics*.  
549 Geological Society of London Special Publication, vol. 45, p. 265–283.

550 Doglioni, C., 1991. A proposal for the kinematic modelling of W-dipping subductions - Possible  
551 applications to the Tyrrhenian-Apennines system. *Terra Nova*, vol. 3, n. 4, p. 423–434.

552 Duffy, O.B., Nixon, C.W., Bell, R.E., Jackson, C.A.L., Gawthorpe, R.L., Sanderson, D.J., and  
553 Whipp, P.S., 2017. The topology of evolving rift fault networks: single phase vs multi-phase rifts.  
554 *Journal of Structural Geology*, vol. 96, p. 192-202.

555 Elter, P., and Schwab, K., 1959. Note illustrative della Carta Geologica alla scala 1:50.000 della  
556 regione Carro-Zeri-Pontremoli. *Boll. Soc. Geol. It.*, vol. 78, p. 157-187.

557 Elter, P., and Pertusati, P., 1973. Considerazioni sul limite Alpi-Appennino e sulle relazioni con  
558 l'arco delle Alpi occidentali. *Mem. Soc. Geol. It.*, vol. 12, p. 359-375.

559 Elter, P., Giglia, G., Tongiorgi, M., and Trevisan, L., 1975. Tensional and compressional areas in  
560 recent (Tortonian to present) evolution of Northern Apennines. *Boll. Geofis. Teor. Appl*, vol. 17, p.  
561 13-18.

562 Faulkner, D., Jackson, C., Lunn, R., Schlische, R., Shipton, Z., Wibberley, C., and Withjack, M.,  
563 2010. A review of recent developments concerning the structure, mechanics and fluid flow  
564 properties of fault zones. *Journal of Structural Geology*, vol. 32, p. 1557-1575.

565 Faulkner, D.R., Mitchell, T.M., Jensen, E., and Cembrano, J., 2011. Scaling of fault damage zones  
566 with displacement and the implications for fault growth processes. *Journal of Geophysical*  
567 *Research*, vol. 116, B05403.<http://dx.doi.org/10.1029/2010JB007788>.

568 Federici, P.R., 1978. La tettonica recente dell'appennino; 2) Il bacino fluvio-lacustre di Pontremoli  
569 (Alta Val di Magra) e sue implicazioni neotettoniche. *G.S.Q.P., Quaderno n. 4*, p. 121-131.

570 Gupta, A., and Scholz, C.H., 2000. A model of normal fault interaction based on observations and  
571 theory. *Journal Structural Geology*, vol. 22, p. 865-879.

572 Hardy, S., and McClay, K., 1999. Kinematic modeling of extensional fault propagation folding.  
573 Journal of Structural Geology, vol. 21, p. 695-702, [https:// doi .org /10.1016 /S0191 -8141](https://doi.org/10.1016/S0191-8141(99)00072-3)  
574 (99)00072-3.

575 Healy, D., Rizzo, R.E., Cornwell, D.G., Farrell, N.J., Watkins, H., Timms, N.G., Gomez-Rivas, E.,  
576 and Smith, M., 2016. FracPaQ: a MATLAB toolbox for the quantification of fracture patterns.  
577 Journal of Structural Geology, vol. 95, p. 1-16.

578 Hudson, J.A., and Priest, S.D., 1979. Discontinuities and rock mass geometry. Int. J. Mech. Min.  
579 Sci. Geomech. Abstr., vol. 16, p. 339-362.

580 Jenkins, C., Ouenes, A., Zellou, A., and Wingard, J., 2009. Quantifying and predicting naturally  
581 fractured reservoir behavior with continuous fracture models. AAPG Bulletin, vol. 93 (11), p. 1597-  
582 1608.

583 Jin, G., and Groshong, R.H., Jr., 2006. Trishear kinematic modelling of extensional fault-  
584 propagation folding. Journal of Structural Geology, vol. 28, p. 170-183, [https:// doi .org /10 .1016](https://doi.org/10.1016/j.jsg.2005.09.003)  
585 /j.jsg .2005 .09 .003.

586 Jolivet, L., Faccenna, C., Goffé, B., Mattei, M., Rossetti, F., Brunet, C., Storti, F., Funicello, R.,  
587 Cadet, J.P., D'Agostino, N., and Parra, T., 1998. Midcrustal shear zones in postorogenic extension:  
588 Example from the northern Tyrrhenian Sea. Journal of Geophysical Research, vol. 103, p. 12,123–  
589 12,160.

590 Kim, Y.S., Peacock, D.C.P., and Sanderson, D.J., 2004. Fault damage zones. Journal of Structural  
591 Geology, vol. 26 (3), p. 503-517.

592 Knott, S.D., Beach, A., Brockbank, P.J., Brown, J.L., McCallum, J.E., and Welbon, A.I., 1996.  
593 Spatial and mechanical controls on normal faultpopulations. Journal of Structural Geology, vol. 18,  
594 p. 359-372.

595 Lucca, A., Storti, F., Molli, G., Mucchez, P., Schito, A., Artoni, A., Balsamo, F., Corrado, S., and  
596 Salvioli Mariani, E., 2018. Seismically-enhanced hydrothermal plume advection through the  
597 process zone of the Compione extensional Fault, Northern Apennines, Italy. Geological Society of  
598 America Bulletin, vol. 131 (3-4), p. 547-571, <https://doi.org/10.1130/B32029.1>.

599 Maerten, L., and Maerten, F., 2006. Chronologic modeling of faulted and fractured reservoirs using  
600 geomechanically based restoration: Technique and industry applications. AAPG Bulletin, vol. 90, p.  
601 1201-1226.

602 Malinverno, A., and Ryan, W.B.F., 1986. Extension in the Tyrrhenian Sea and shortening in the  
603 Apennines as result of arc migration driven by sinking of the lithosphere. *Tectonics*, vol. 5, p. 227-  
604 245.

605 Mandl, G., 2000. *Faulting in brittle rocks: an introduction to the mechanics of tectonic faults*.  
606 Springer-Verlag, Heidelberg, Berlin.

607 Manzocchi, T., 2002. The connectivity of two dimensional networks of spatially correlated  
608 fractures. *Water Resources, Res.* 38, <http://dx.doi.org/10.1029/2000WR000180>.

609 Martini, I.P., Sagri, M., and Colella, A., 2001. Neogene-Quaternary basins of the inner Apennines  
610 and Calabrian arc. In: *Anatomy of an orogeny: The Apennines and adjacent Mediterranean Basins*,  
611 edited by Vai G.B. and Martini I.P., p. 375-400, Kluwer Acad., Dordrecht, Netherlands.

612 Mauldon, M., 1998. Estimating mean fracture trace length and density from observations in convex  
613 windows. *Rock Mechanics and Rock Engineering*, vol. 31, p. 201-216.

614 McGrath, A.G., and Davison, I., 1995. Damage zone geometry around fault tips. *Journal of*  
615 *Structural Geology*, vol. 17 (7), p. 1011-1024.

616 Micarelli, L., Moretti, I., and Daniel, J.M., 2003. Structural properties of rift-related normal faults:  
617 the case study of the Gulf of Corinth, Greece. *Journal of Geodynamics*, vol. 36, p. 275-303.

618 Micarelli, L., Benedicto, A., and Wibberley, C.A.J., 2006. Structural evolution and permeability of  
619 normal fault zones in highly porous carbonate rocks. *Journal of Structural Geology*, vol. 28 (7), p.  
620 1214-1227.

621 Molli, G., Carlini, M., Vescovi, P., Artoni, A., Balsamo, F., Camurri, F., Clemenzi, L., Storti, F.,  
622 and Torelli, L., 2018. Neogene 3D-structural architecture of the north-west Apennines: the role of  
623 the low angle normal faults and basement thrusts. *Tectonics*, vol. 37, p. 2165-2196.

624 Morley, C.K., and Nixon, C.W., 2016. Topological characteristics of simple and complex normal  
625 fault networks. *J. Struct. Geol.*, vol. 84, p. 68-84.

626 Nelson, R.A., 1985. *Geologic Analysis of Naturally Fractured Reservoirs*, Gulf, Houston, Tex., 320  
627 p.

628 Nixon, C.W., Sanderson, D.J., Bull, J.M., 2011. Deformation within a strike-slip fault network at  
629 Westward Ho!, Devon U.K.: domino vs conjugate faulting. *Journal of Structural Geology*, vol. 33,  
630 p. 833-843.

631 Nixon, C.W., Sanderson, D.J., and Bull, J.M., 2012. Analysis of a strike-slip fault network using  
632 high resolution multibeam bathymetry, offshore NW Devon U.K. *Tectonophysics*, vol. 541-543, p.  
633 69-80.

634 Nixon, C.W., Sanderson, D.J., Dee, S., Bull, J.M., Humphreys, R., and Swanson, M., 2014. Fault  
635 interactions and reactivation within a normal fault network at Milne Point, Alaska. *Am. Assoc. Pet.*  
636 *Geol. Bull.*, vol. 98, p. 2081-2107.

637 Odling, N.E., Gillespie, P., Bourguine, B., Castaing, C., Chilés, J-P., Christensen, N.P., Fillion, E.,  
638 Genter, A., Olsen, C., Thrane, L., Trice, R., Arseth, E., Walsh, J., and Watterson, J., 1999.  
639 Variations in fracture system geometry and their implications for fluid flow in fractured  
640 hydrocarbon reservoirs. *Petroleum Geoscience*, vol. 5, p. 373-384.

641 Peacock, D.C.P., Dimmen, V., Rotevatn, A., and Sanderson, D.J., 2017. A broader classification of  
642 damage zones. *Journal of Structural Geology*, vol. 102, p. 179-192.

643 Perrin, C., Manighetti, I., Ampuero, J.P., Cappa, F., and Gaudemer, Y., 2016. Location of largest  
644 earthquake slip and fast rupture controlled by along-strike change in fault structural maturity due to  
645 fault growth. *J. Geophys. Res. Solid Earth*, vol. 121, p. 3666-3685.

646 Pickering, G., Bull, J.M., and Sanderson, D.J., 1995. Sampling power-law distributions.  
647 *Tectonophysics*, vol. 248, p. 1-20.

648 Principi, G., and Treves, B., 1984. Il sistema corso-appennino come prisma d'accrescimento. *Riflessi*  
649 *sul problema generale del limite Alpi-Appennino*. *Memorie della Società Geologica Italiana*, vol.  
650 28, p. 529-576.

651 Procter, A., and Sanderson, D.J., 2018. Spatial and layer-controlled variability in fracture networks.  
652 *J. Struct. Geol.*, vol. 108, p. 52-65.

653 Raggi, G., 1985. Neotettonica ed evoluzione paleogeografica plio-pleistocenica del Bacino de fiume  
654 Magra. *Memorie della Società Geologica Italiana*, vol. 30, p. 35-62.

655 Robinson, P.C., 1983. Connectivity of fracture systems-a percolation theory approach. *J. Phys. A:*  
656 *Math. Gen.*, vol. 16, p. 605-614.

657 Robinson, P.C., 1984. Numerical calculations of critical densities for lines and planes. *J. Phys. A:*  
658 *Math. Gen.*, vol. 17, p. 2823-2830.

659 Royden, L., 1988. Flexural behaviour of the continental lithosphere in Italy: Constraints imposed by  
660 gravity and deflection data. *Journal of Geophysical Research*, vol. 93, p. 7747-7766.

661 Sanderson, D.J., and Nixon, C.W., 2015. The use of topology in fracture network characterization.  
662 Journal of Structural Geology, vol. 72, p. 55-66.

663 Sanderson, D.J., and Nixon, C.W., 2018. Topology, connectivity and percolation in fracture  
664 networks. J. Struct. Geol., vol. 115, p. 167-177.

665 Savage, H.M., and Brodsky, E.E., 2011. Collateral damage: evolution with displacement of fracture  
666 distribution and secondary fault strands in fault damage zones. Journal of Geophysical Research,  
667 vol. 116, B03405.

668 Schlische, R.W., Young, S.S., Ackermann, R.V. and Gupta, A., 1996. Geometry and scaling of a  
669 population of very small rift-related normal faults, Geology, vol. 24, p. 683-686.

670 Shipton, Z.K., and Cowie, P.A., 2003. A conceptual model for the origin of fault damage zone  
671 structures in high-porosity sandstone. Journal of Structural Geology, vol. 25 (8), p. 1343-1345.

672 Soliva, R., and Benedicto, A., 2005. Geometry, scaling relations and spacing of vertically restricted  
673 normal faults. Journal of Structural Geology, vol. 27 (2), p. 317-325.

674 Storti, F., 1995. Tectonics of the Punta Bianca promontory: Insights for the evolution of the  
675 Northern Apennines-Northern Tyrrhenian Sea basin. Tectonics, vol. 14, p. 832-847.

676 Tinti, E., Spudich, P., and Cocco, M., 2005. Earthquake fracture energy inferred from kinematic  
677 rupture models on extended faults. J. Geophys. Res., vol. 110, B12303, doi:10.1029/2005JB003644.

678 Torabi, A., and Berg, S.S., 2011. Scaling of fault attributes: a review. Marine and Petroleum  
679 Geology, vol. 28, p. 1444-1460.

680 Torabi, A., Ellingsen, T.S.S., Johannessen, M.U., Alaei, B., Rotevatn, A., and Chiarella, D., 2019.  
681 Fault zone architecture and its scaling laws: where does the damage zone start and stop? Geological  
682 Society, London, Special Publications, 496, <https://doi.org/10.1144/SP496-2018-151>.

683 Vermilye, J.M., and Scholz, C.H., 1998. The process zone: a microstructural view of fault growth.  
684 Journal of Geophysical Research: Solid Earth, vol. 103 (B6), p. 12223-12237.

685 Vescovi, P., 2005. The Middle Miocene Mt. Ventasso – Mt. Cimone arcuate structure of the Emilia  
686 Apennines. Bollettino della Società Geologica Italiana, vol. 124, p. 53-67.

687 Walsh, J.J., Bailey, W.R., Childs, C., Nicol, A., and Bonson, C.G., 2003. Formation of segmented  
688 normal faults: a 3-D perspective. Journal of Structural Geology, vol. 25, p. 1251-1262.

689 Zeeb, C., Gomez-Rivas, E., Bons, P.D., and Blum, P., 2013. Evaluation of sampling methods for  
690 fracture network characterization using outcrops. *Am. Assoc. Pet. Geol. Bull.*, vol. 97(9), p. 1545-  
691 1566.

## 692 **Figure Captions**

693 **Figure 1:** (A) Simplified structural geologic map of the Tyrrhenian Sea side of the Northern Apennines (modified  
694 from Bernini et al., 1997). The Compione Fault belongs to the Northern Lunigiana Extensional Fault System and  
695 is indicated in white. Inset indicates location of A. (B) Regional geologic-cross section (A-A') showing the  
696 Northern Apennines orogenic wedge tectonic architecture (modified from Molli et al., 2018).

697 **Figure 2:** (A) Geologic map of the study area showing locations of circular scan windows in the footwall of the  
698 Compione Fault, which are indicated by white dots, along with bedding attitudes and subsidiary fault zones. The  
699 black line with rhombs indicates the position of the extensional fault propagation fold hinge zone. (B) Cross-  
700 section illustrating the structural architecture of the Compione footwall damage zone with projected locations of  
701 circular windows, grouped into structural sectors. (C) Cumulative apparent dip data of early (black) and late  
702 fractures (grey) plotted in a half-rose diagram. (D) Early fractures dip values in C after bedding restoration to the  
703 horizontal. (E-F-G) Outcrop pictures showing representative fault-related fracture patterns for structural sectors 1,  
704 4 and 6, respectively.

705 **Figure 3:** Workflow of this study. (A) Selected SSW-NNE oriented wall exposure of thick-bedded Macigno Fm.  
706 sandstones strata and 25 cm radius circle drawn on the outcrop to take a properly oriented and scaled picture. (B)  
707 Poles and density contour of poles (c.i.: 1%) to fractures showing 3D orientations and range of vertical scan  
708 window planes, indicated by the striped area. (C) Digitized fracture traces inside the circle using straight  
709 segments. (D) Counting I (circles), X (squares) and Y (triangles) nodes inside the circular window and fracture  
710 intersections with the circumference (crosses). (E) Area weighted fracture dips extracted from the digitized  
711 fracture trace map using FracPaQ2D (Healy et al., 2017).

712 **Figure 4:** Digitized fracture traces inside circular windows from photographs acquired on vertical, SSW-NNE  
713 oriented, outcrops of Macigno Fm. sandstones thick strata. Dashed lines in windows from 30 to 35 represent  
714 fractures that opened along primary sedimentary bedding anisotropies and thick lines in windows from 1 to 20  
715 indicate late fractures. Scan window number is shown to the right and distance from the fault core to the left of  
716 each circular window.

717 **Figure 5:** (A) Fracture dip values in half-rose diagrams grouped by structural sectors (distance from fault core in  
718 meters is also reported). Late fractures are in white. (B) Early fracture dip data shown in A are rotated by restoring  
719 bedding attitude to the horizontal. Dip values belonging to structural sector 6 are not restored since they are  
720 assumed not to be affected by rotation. (C) Rose diagrams after an additional 10° clockwise rotation of sites 2 to  
721 5.

722 **Figure 6:** (A) Dip values of fractures from circular windows, plotted in half-rose diagrams. Grey bars indicate  
723 mean bedding attitude for each structural sector. Half-rose diagrams in the same column belong to the same

724 structural sector. Colored bars (black numbered axis) represent early fractures while late fractures are in white  
725 (grey numbered axis). (B) Cross-section of Fig. 2B.

726 **Figure 7:** The left column shows mean values and  $\pm 1$  standard deviation of structural sectors while in the right  
727 column singular scan windows values are reported. (A-B) Plots of  $P_{21}$  and  $P_{10}$  vs. distance from the fault core. (C-  
728 D) Plots of  $P_{20}$  (black) and  $B_{20}$  (grey) vs. distance from the fault core. (E-F) Plots of  $P_{22}$  vs. distance from the fault  
729 core. (G-H) Plots of  $B_{22}$  vs. distance from the fault core. Negative dip values indicate bedding dipping towards  
730 NNE, while positive towards the fault core, i.e. SSW.

731 **Figure 8:** (A) Triangular plot showing relative percentage of I, X and Y nodes per circular window (circles) and  
732 per structural sector (stars). Number of connections per fracture (red) and per branch (blue) are also shown. (B)  
733 Triangular plot showing relative percentage of of I-I, I-C and C-C branches per circular window.

734 **Figure 9:** Plots showing number of nodes vs. distance from the fault core. (A) Total number of nodes ( $I + X + Y$ )  
735 vs. distance from the fault core. (B) Number of I nodes vs. distance from the fault core. (C) Number of X nodes  
736 vs. distance from the fault core. (D) Number of Y nodes vs. distance from the fault core.

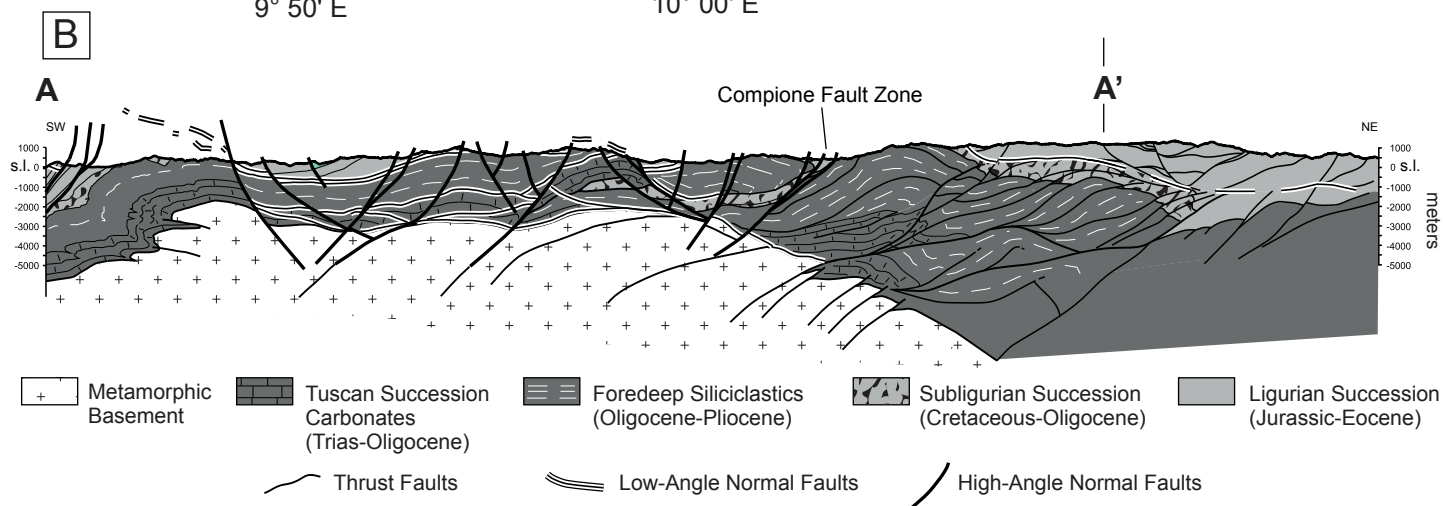
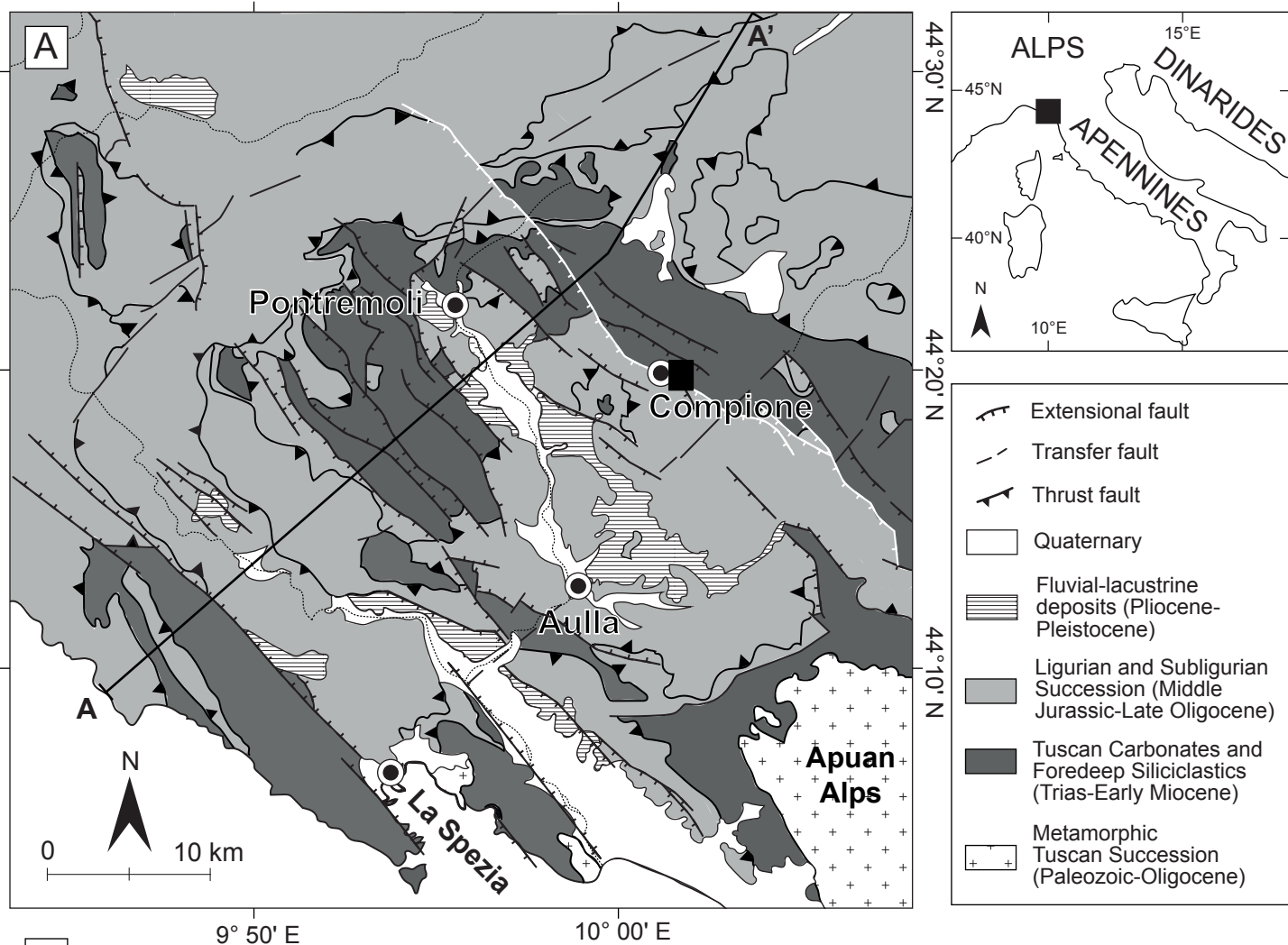
737 **Figure 10:** Plots of number of nodes vs. fracture intensity (equation 5). (A) Total number of nodes ( $I + X + Y$ ) vs.  
738 fracture intensity. (B) Number of I nodes vs. fracture intensity. (C) Number of X nodes vs. fracture intensity. (D)  
739 Number of Y nodes vs. fracture intensity.

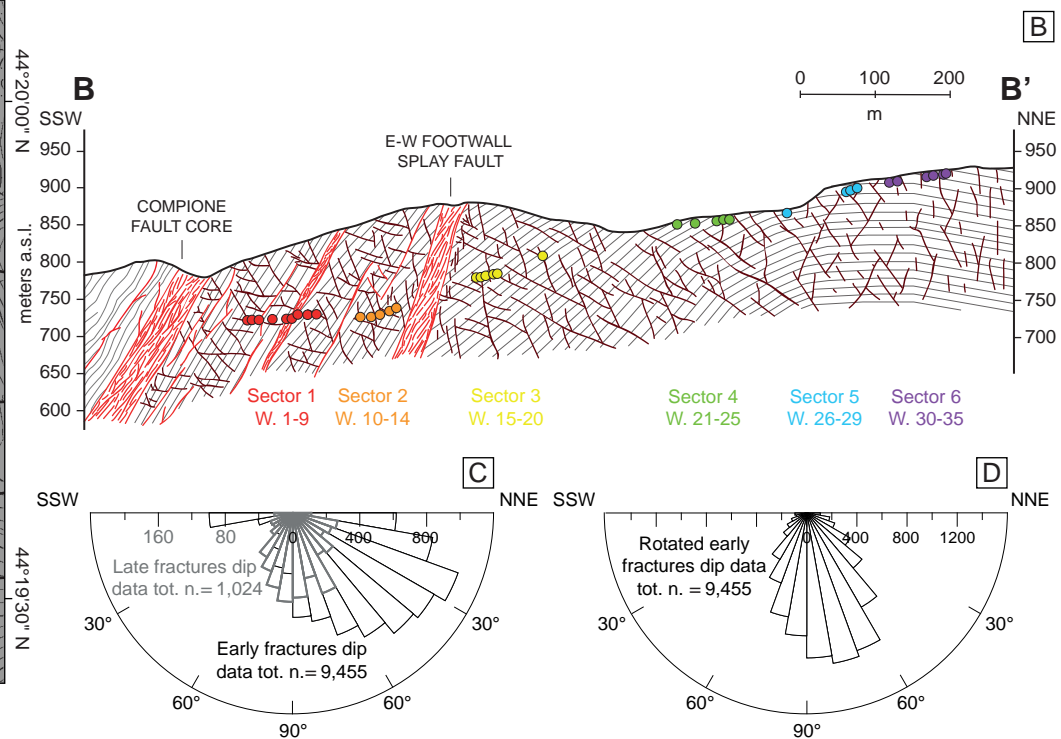
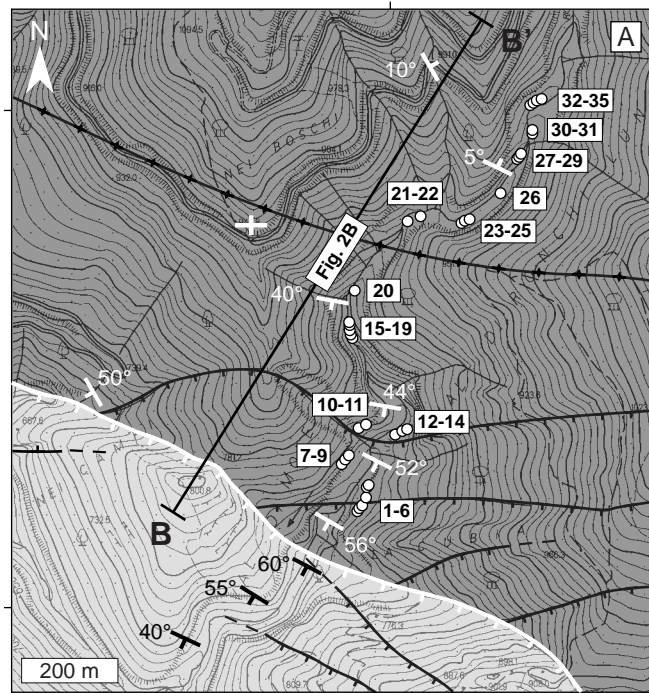
740 **Figure 11:** (A) Summary plots showing mean values (thick lines) and  $\pm 1\sigma$  (thin lines) of  $P_{21}$  and  $P_{10}$  (solid black  
741 line & dashed black, respectively), fracture frequency (light grey) and branch frequency (dark grey) vs. distance  
742 from the fault core, grouped by structural sector; bedding dip values are also represented on the horizontal axis.  
743 (B) Same plot as in (A), showing dimensionless fracture intensity (black) and dimensionless branch intensity  
744 (dark grey). (C) Same plot as in (A) and (B), showing numbers of Y nodes (black), X nodes (dark grey) and I  
745 nodes (light grey) per square meter.

746 **Figure 12:** Histograms of fracture dip values grouped by structural sector, showing standard deviation values  
747 (SD) assuming a normal statistical distribution.

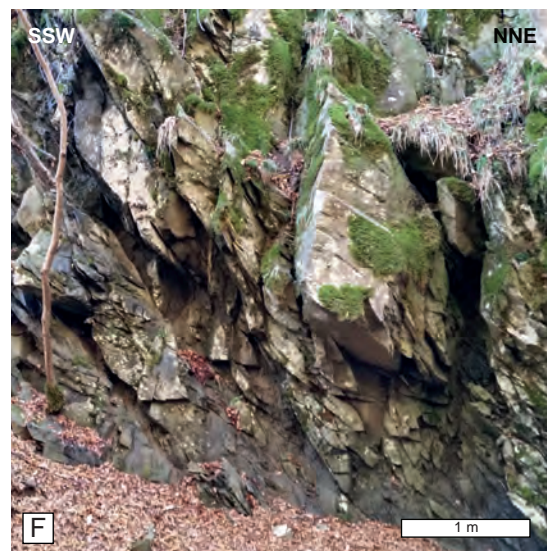
748 **Figure 13:** Conceptual model of damage zone evolution during extensional fault propagation: (A) initial tip  
749 damage zone formation and early fractures nucleation; (B) localization of deformation in the wall damage zone,  
750 re-activation of early fractures, and nucleation of late fractures after passive extensional folding. Rose diagrams  
751 grouped by structural sector show early (grey) and late (black) fracture dip directions. The grey area in the left  
752 corner represents the Compione fault core, while the thin grey area schematically indicates the major E-W  
753 footwall splay fault zone.







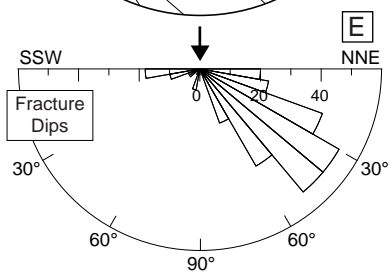
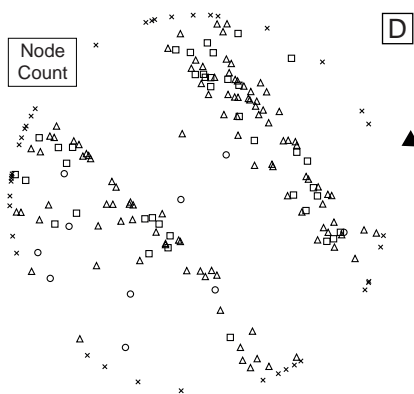
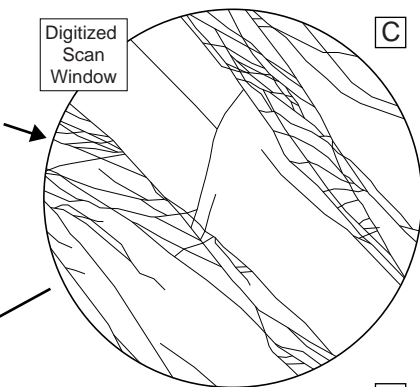
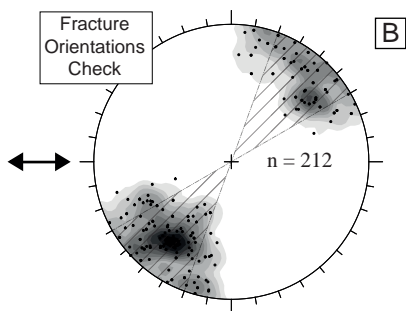
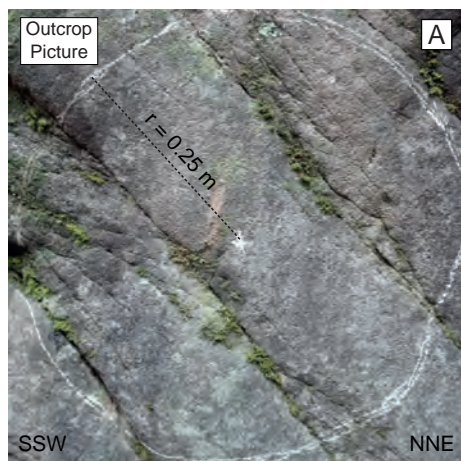
STRUCTURAL SECTOR 1



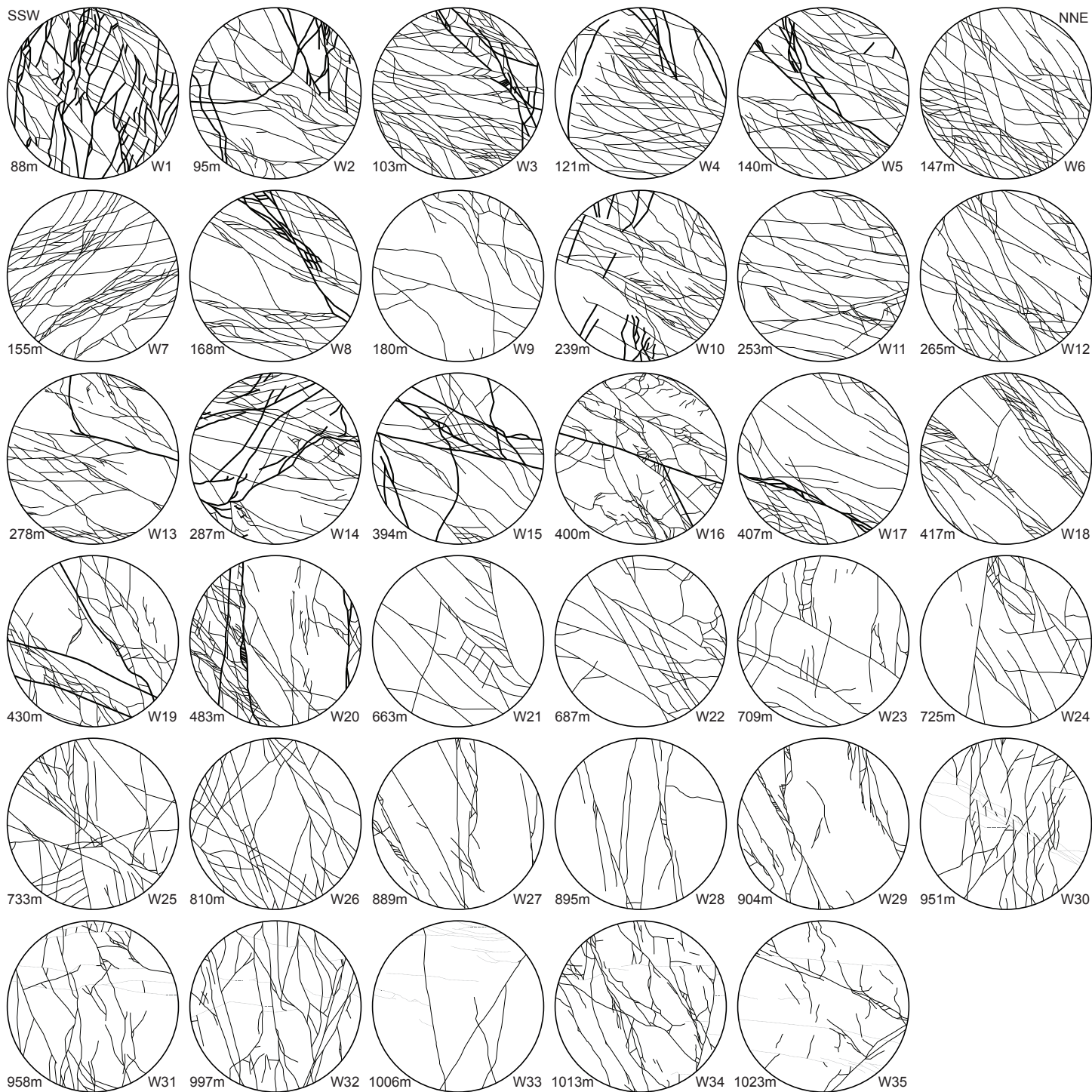
STRUCTURAL SECTOR 4

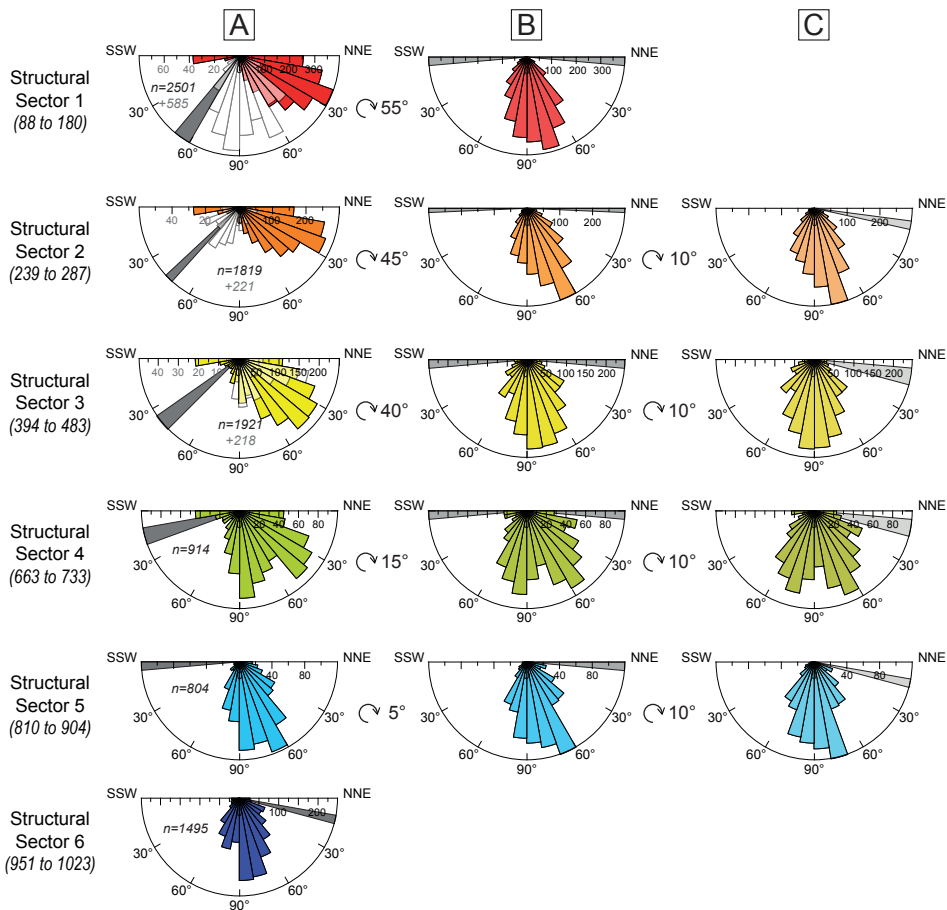


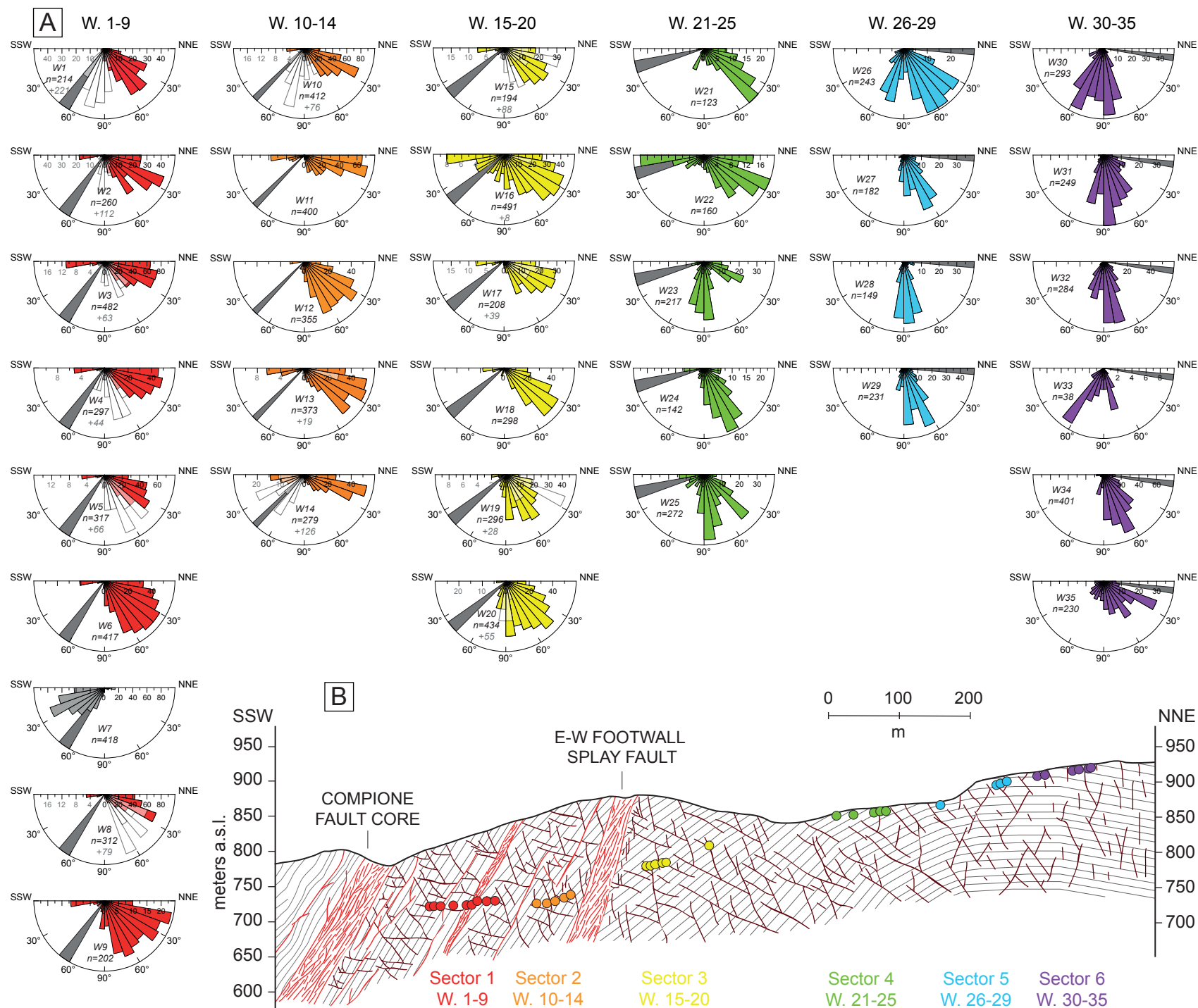
STRUCTURAL SECTOR 6

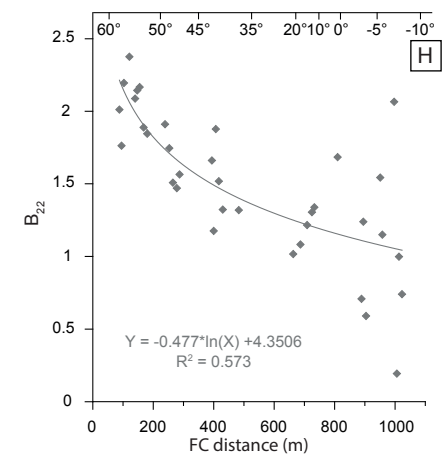
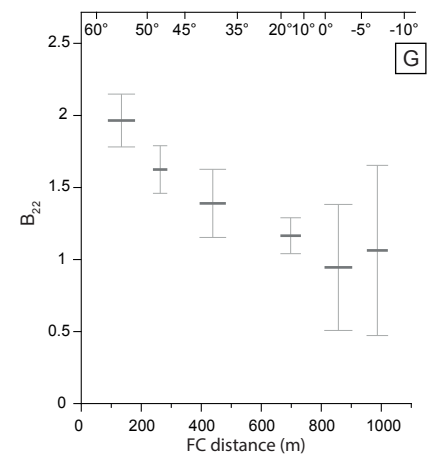
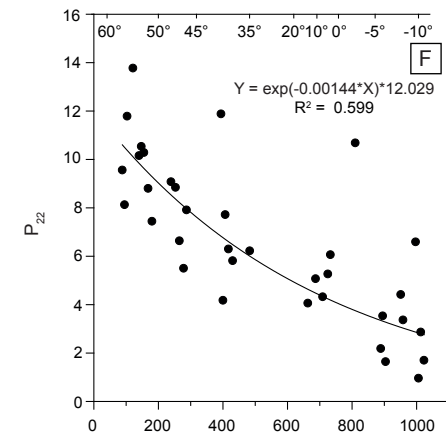
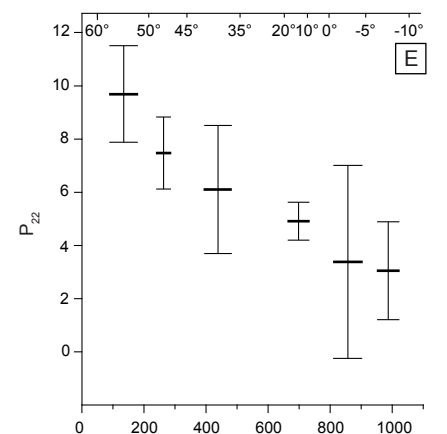
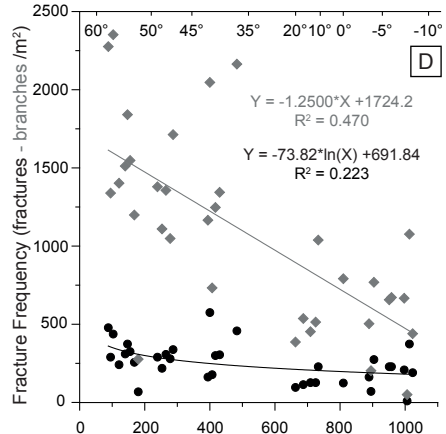
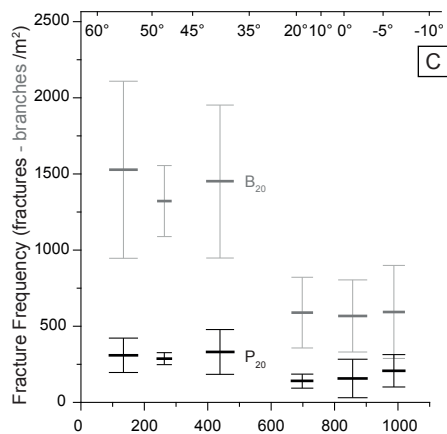
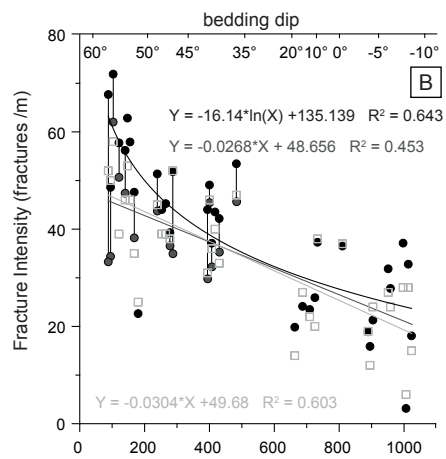
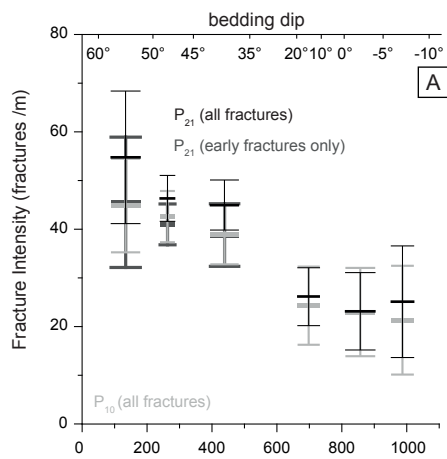


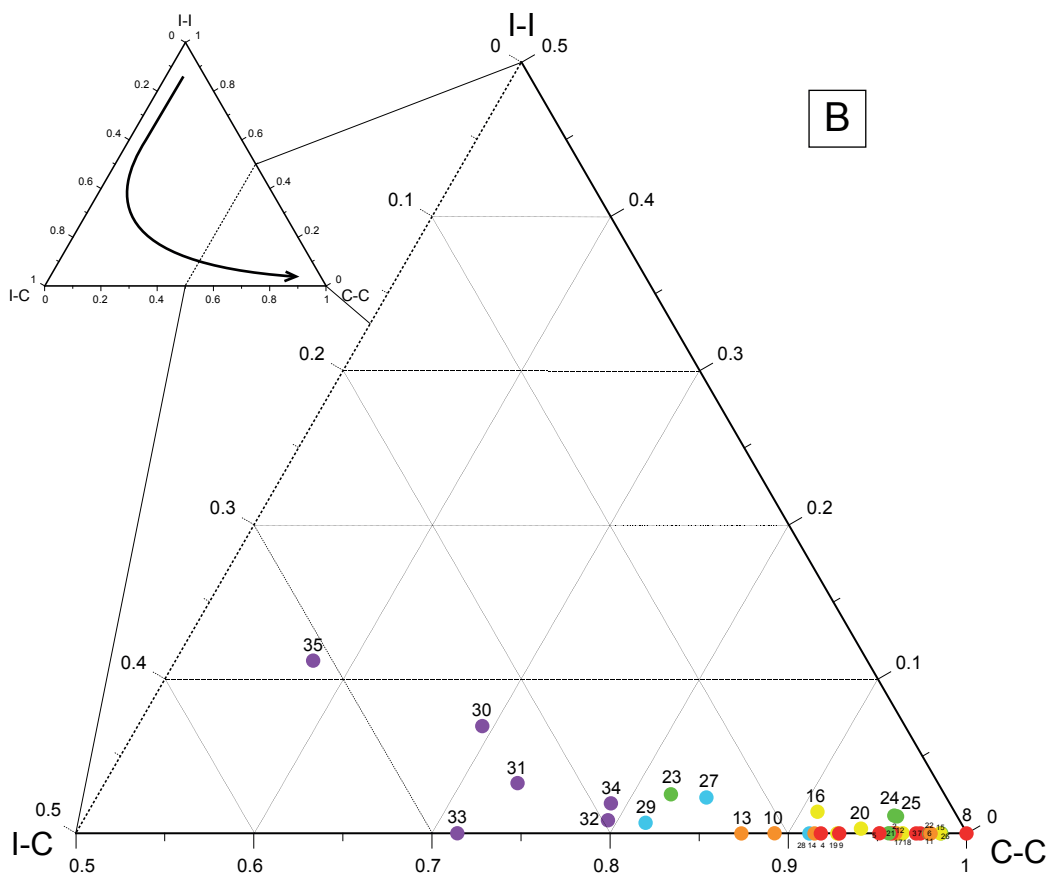
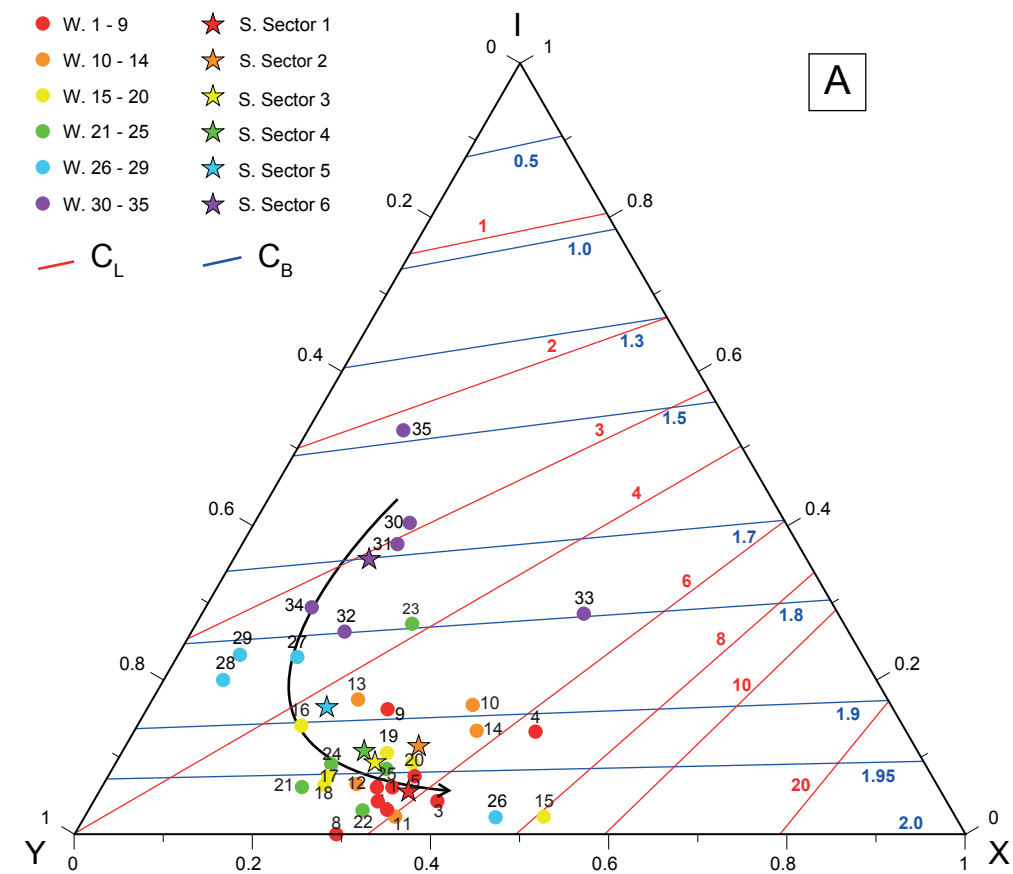




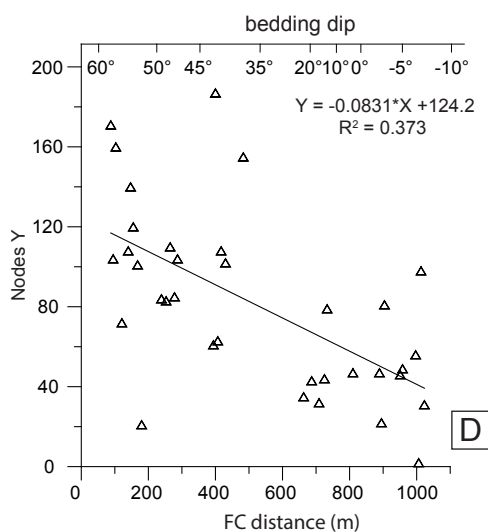
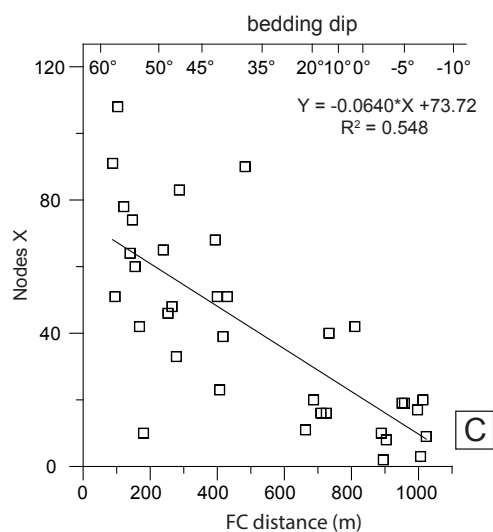
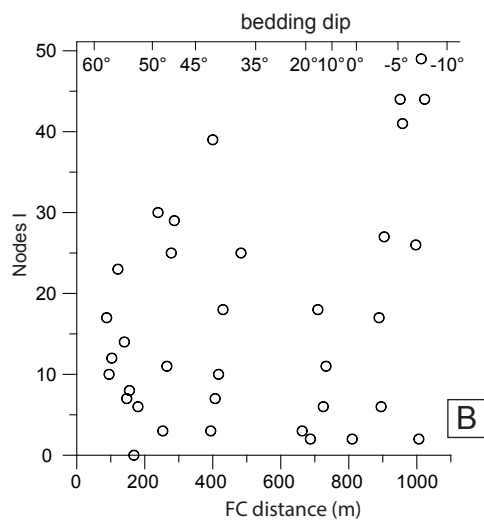
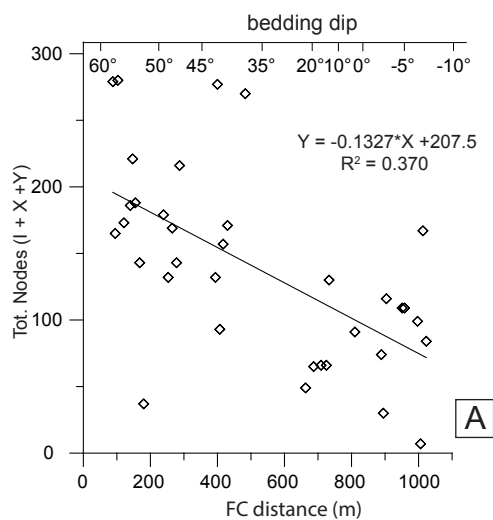


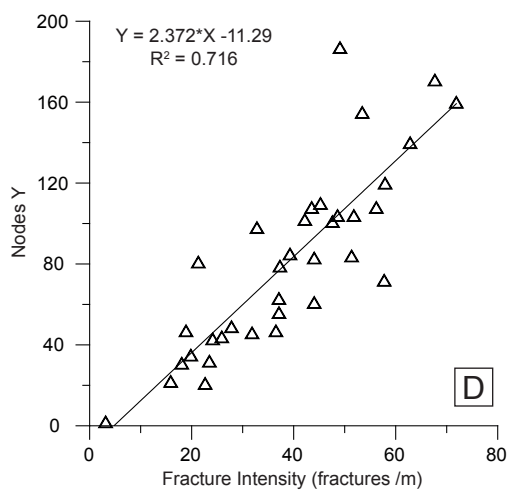
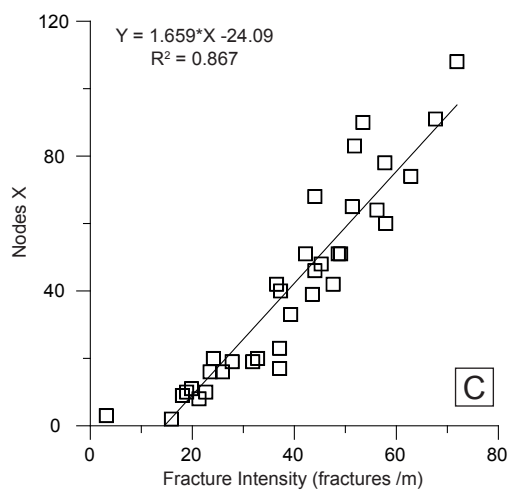
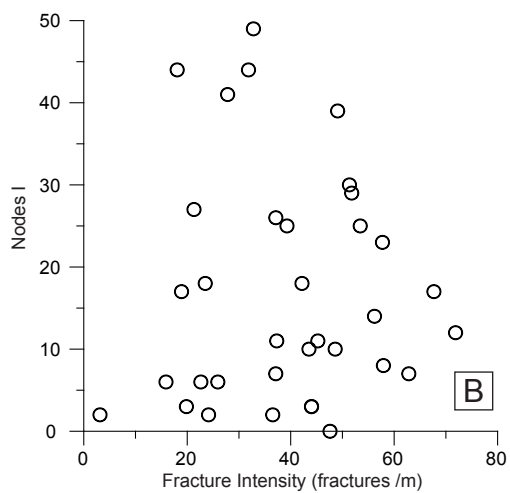
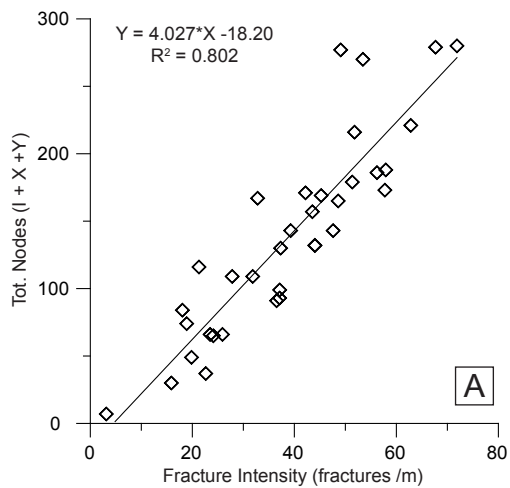


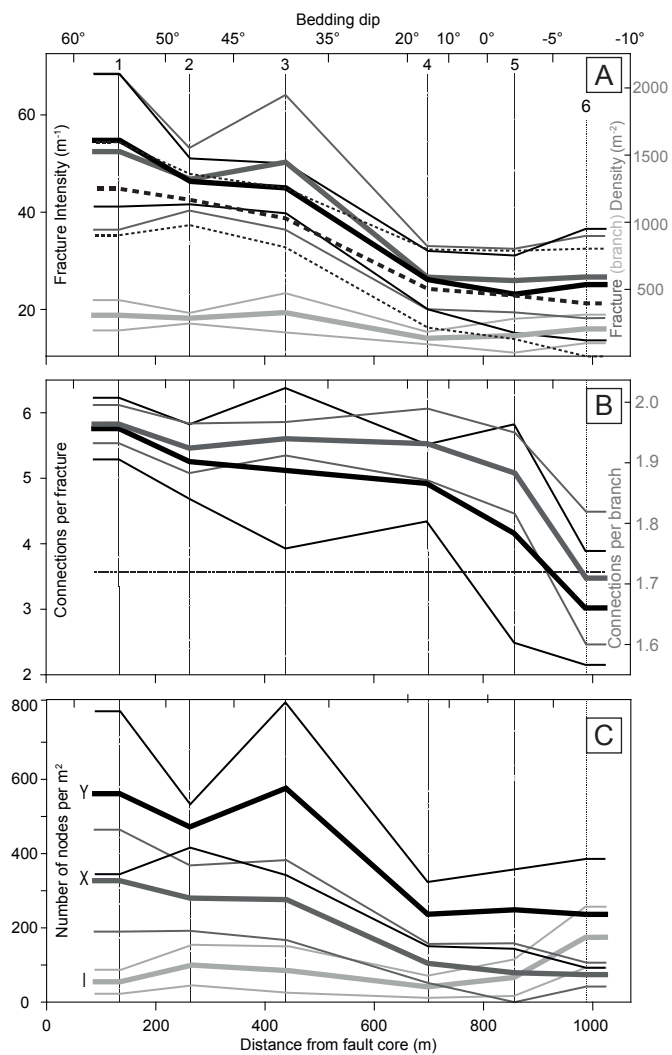


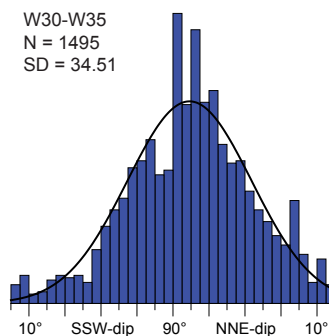
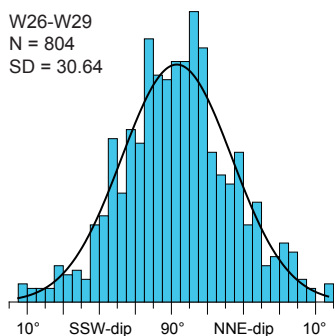
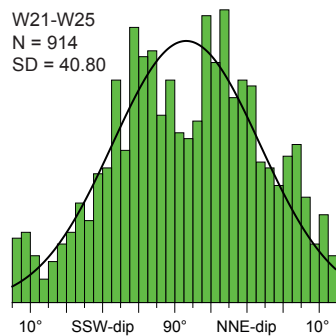
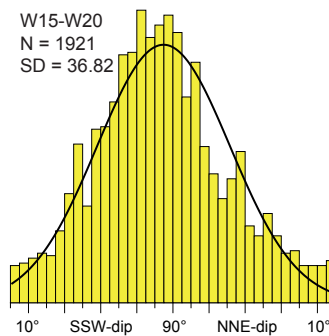
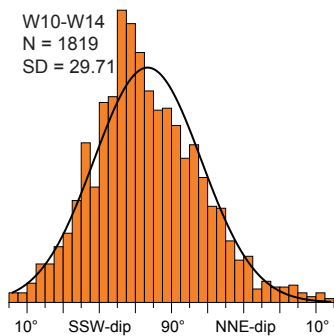
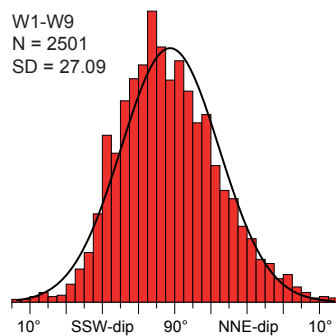












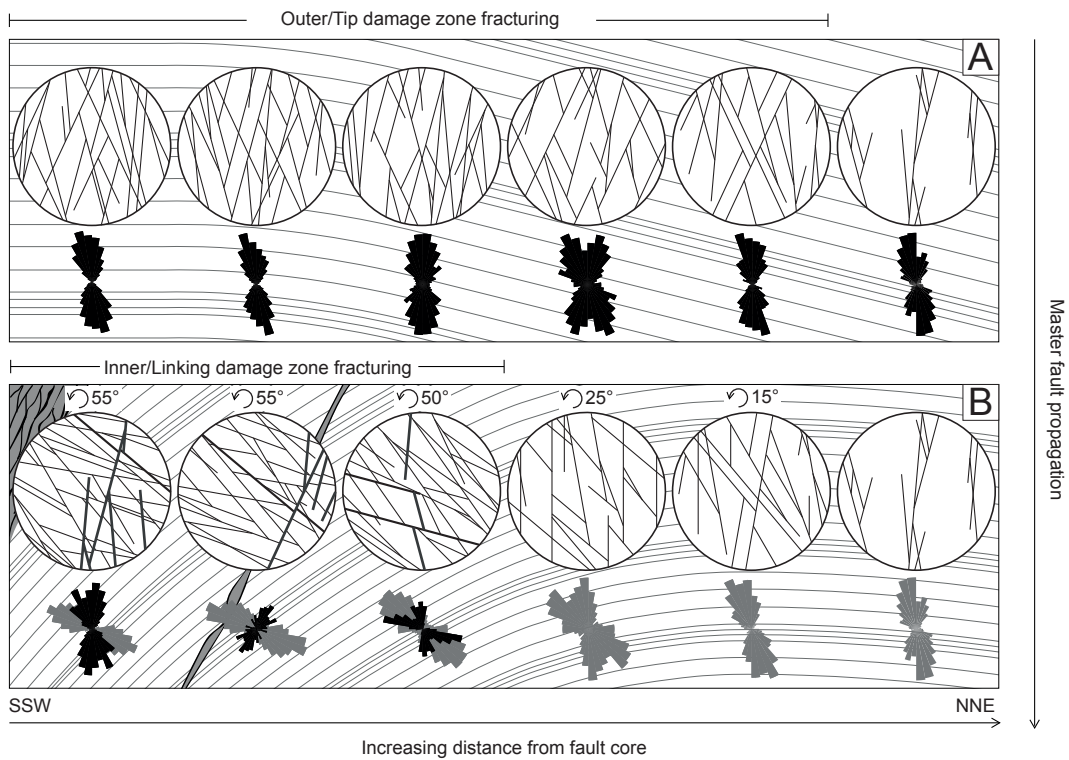


**Table 1: Mean values of topological and fracture attributes per structural sector.**

<b>Scan Windows</b>	<b>1 to 9</b>	<b>10 to 14</b>	<b>15 to 20</b>	<b>21 to 25</b>	<b>26 to 29</b>	<b>30 to 35</b>
d. (m)	88 to 180	239 to 287	394 to 663	687 to 733	810 to 904	951 to 1023
I	10.78	19.60	17.00	8.00	13.00	34.33
X	64.22	55.00	53.67	20.60	15.50	14.50
Y	110.78	93.20	112.67	46.60	49.25	47.00
Nodes	185.78	167.80	183.33	75.20	77.75	95.83
P <sub>I</sub> (%)	5.80	11.68	9.27	10.64	16.72	35.83
P <sub>X</sub> (%)	34.57	32.78	29.27	27.39	19.94	15.13
P <sub>Y</sub> (%)	59.63	55.54	61.45	61.97	63.34	49.04
I-I	0.00	0.00	1.00	1.00	0.75	4.17
I-C	9.89	18.00	14.33	5.20	10.25	23.33
C-C	264.89	221.00	248.17	96.20	88.25	77.17
Branches	274.78	239.00	263.50	102.40	99.25	104.67
P <sub>I-I</sub> (%)	0.00	0.00	0.38	0.98	0.76	3.98
P <sub>I-C</sub> (%)	3.60	7.53	5.44	5.08	10.33	22.29
P <sub>C-C</sub> (%)	96.40	92.47	94.18	93.95	88.92	73.73
N <sub>L</sub>	60.8	56.4	64.8	27.3	31.1	40.7
N <sub>B</sub>	300	260	285	115	111	117
N <sub>B</sub> /N <sub>L</sub>	4.94	4.60	4.39	4.22	3.58	2.87
ΣL	10.76	9.10	8.82	5.13	4.55	4.93
P <sub>20</sub>	310	287	330	139	159	207
B <sub>20</sub>	1528	1322	1451	586	567	594
P <sub>21</sub>	54.8	46.3	44.9	26.1	23.2	25.1
P <sub>10</sub>	44.9	42.6	38.8	24.2	23.0	21.3
P <sub>22</sub>	9.70	7.48	6.10	4.91	3.38	3.05
B <sub>22</sub>	1.96	1.62	1.39	1.16	0.95	1.06
C <sub>L</sub>	5.76	5.26	5.13	4.92	4.16	3.02
C <sub>B</sub>	1.96	1.92	1.94	1.93	1.88	1.71

## Conflict of Interest and Authorship Conformation Form

Please check the following as appropriate:

- ☐ All authors have participated in (a) conception and design, or analysis and interpretation of the data; (b) drafting the article or revising it critically for important intellectual content; and (c) approval of the final version.
- ☐ This manuscript has not been submitted to, nor is under review at, another journal or other publishing venue.
- ☐ The authors have no affiliation with any organization with a direct or indirect financial interest in the subject matter discussed in the manuscript
- ☐ The following authors have affiliations with organizations with direct or indirect financial interest in the subject matter discussed in the manuscript:

Author's name

Affiliation

Alessio Lucca

Università degli Studi di Parma

---

---

---

---

---

---

---

---

Conceptualization:	AL	FS	GM	
Methodology:	AL	FS		
Software:	AL			
Validation:	AL	FS	GM	
Formal analysis:	AL	FS	GM	
Investigation:	AL	FS	GM	
Resources:	AL	FS	GM	
Data Curation:	AL	FS	GM	
Writing:	AL	FS	GM	
Writing - Review & Editing:	AL	FS	GM	
Visualization:	AL	FS	GM	
Supervision:		FS	GM	
Project administration:		FS	GM	
Funding acquisition:		FS		



Supporting information for

*Journal of Structural Geology*

**Extensional fracture network attribute distribution in faulted thick sandstone  
strata: Compione Fault, Northern Apennines, Italy**

Alessio Lucca<sup>1</sup>, Fabrizio Storti<sup>1</sup>, Giancarlo Molli<sup>1,2</sup>

<sup>1</sup>*NEXT - Natural and Experimental Tectonics research group, Department of Chemistry, Life Sciences and Environmental Sustainability, University of Parma, I-43124 Parma, Italy*

<sup>2</sup>*Department of Earth Sciences, University of Pisa, via S. Maria, 53, I-56126 Pisa, Italy*

**Contents of this file**

Supplementary Table 1

**Introduction**

This supporting information provides values of calculated fracture attributes for each scan window

**Supplementary Table 1: List of topological and fracture attribute values per scan window.**

W.	d. (m)	I	X	Y	Nodes	P <sub>I</sub> (%)	P <sub>X</sub> (%)	P <sub>Y</sub> (%)	I-I	I-C	C-C	Branches	P <sub>I-I</sub> (%)	P <sub>I-C</sub> (%)	P <sub>C-C</sub> (%)
1	88	17	91	171	279	6.09	32.62	61.29	0	16	399	415	0.00	3.86	96.14
2	95	10	51	104	165	6.06	30.91	63.03	0	10	227	237	0.00	4.22	95.78
3	103	12	108	160	280	4.29	38.57	57.14	0	12	413	425	0.00	2.82	97.18
4	121	23	78	72	173	13.29	45.09	41.62	0	21	236	257	0.00	8.17	91.83
5	140	14	64	108	186	7.53	34.41	58.06	0	13	257	270	0.00	4.81	95.19
6	147	7	74	140	221	3.17	33.48	63.35	0	7	327	334	0.00	2.10	97.90
7	155	8	60	120	188	4.26	31.91	63.83	0	7	268	275	0.00	2.55	97.45
8	168	0	42	101	143	0.00	29.37	70.63	0	0	218	218	0.00	0.00	100.00
9	180	6	10	21	37	16.22	27.03	56.76	0	3	39	42	0.00	7.14	92.86
10	239	30	65	84	179	16.76	36.31	46.93	0	27	222	249	0.00	10.84	89.16
11	253	3	46	83	132	2.27	34.85	62.88	0	3	195	198	0.00	1.52	98.48
12	265	11	48	110	169	6.51	28.40	65.09	0	10	238	248	0.00	4.03	95.97
13	278	25	33	85	143	17.48	23.08	59.44	0	24	167	191	0.00	12.57	87.43
14	287	29	83	104	216	13.43	38.43	48.15	0	26	283	309	0.00	8.41	91.59
15	394	3	68	61	132	2.27	51.52	46.21	0	3	202	205	0.00	1.46	98.54
16	400	39	51	187	277	14.08	18.41	67.51	5	29	346	380	1.32	7.63	91.05
17	407	7	23	63	93	7.53	24.73	67.74	0	5	120	125	0.00	4.00	96.00
18	417	10	39	108	157	6.37	24.84	68.79	0	8	217	225	0.00	3.56	96.44
19	483	18	51	102	171	10.53	29.82	59.65	0	18	232	250	0.00	7.20	92.80
20	663	25	90	155	270	9.26	33.33	57.41	1	23	372	396	0.25	5.81	93.94
21	687	3	11	35	49	6.12	22.45	71.43	0	3	66	69	0.00	4.35	95.65
22	709	2	20	43	65	3.08	30.77	66.15	0	2	92	94	0.00	2.13	97.87
23	716	18	16	32	66	27.27	24.24	48.48	2	12	64	78	2.56	15.38	82.05
24	725	6	16	44	66	9.09	24.24	66.67	1	3	84	88	1.14	3.41	95.45
25	733	11	40	79	130	8.46	30.77	60.77	2	6	175	183	1.09	3.28	95.63
26	810	2	42	47	91	2.20	46.15	51.65	0	2	136	138	0.00	1.45	98.55
27	889	17	10	47	74	22.97	13.51	63.51	2	12	75	89	2.25	13.48	84.27
28	895	6	2	22	30	20.00	6.67	73.33	0	3	31	34	0.00	8.82	91.18
29	904	27	8	81	116	23.28	6.90	69.83	1	24	111	136	0.74	17.65	81.62
30	951	44	19	46	109	40.37	17.43	42.20	8	27	79	114	7.02	23.68	69.30
31	958	41	19	49	109	37.61	17.43	44.95	4	29	90	123	3.25	23.58	73.17
32	997	26	17	56	99	26.26	17.17	56.57	1	23	93	117	0.85	19.66	79.49
33	1006	2	3	2	7	28.57	42.86	28.57	0	2	5	7	0.00	28.57	71.43
34	1013	49	20	98	167	29.34	11.98	58.68	4	37	155	196	2.04	18.88	79.08
35	1023	44	9	31	84	52.38	10.71	36.90	8	22	41	71	11.27	30.99	57.75

W.	d. (m)	N <sub>L</sub>	N <sub>B</sub>	N <sub>B</sub> /N <sub>L</sub>	ΣL	P <sub>20</sub>	B <sub>20</sub>	P <sub>21</sub>	P <sub>10</sub>	P <sub>22</sub>	B <sub>22</sub>	C <sub>L</sub>	C <sub>B</sub>
1	88	94	447	4.8	13.29	479	2277	67.7	52	9.57	2.01	5.57	1.96
2	95	57	263	4.6	9.54	290	1339	48.6	50	8.14	1.76	5.44	1.96
3	103	86	462	5.4	14.11	438	2353	71.9	58	11.79	2.20	6.23	1.97
4	121	48	276	5.8	11.34	242	1403	57.7	39	13.78	2.38	6.32	1.92
5	140	61	297	4.9	11.03	311	1513	56.2	46	10.17	2.09	5.64	1.95
6	147	74	362	4.9	12.34	374	1841	62.8	53	10.55	2.14	5.82	1.98
7	155	64	304	4.8	11.37	326	1548	57.9	46	10.29	2.17	5.63	1.97
8	168	51	236	4.7	9.35	257	1199	47.6	35	8.81	1.89	5.66	2.00
9	180	14	55	4.0	4.44	69	278	22.6	25	7.45	1.85	4.59	1.89
10	239	57	271	4.8	10.08	290	1380	51.4	45	9.09	1.91	5.23	1.89
11	253	43	218	5.1	8.65	219	1110	44.0	39	8.85	1.75	6.00	1.99
12	265	61	267	4.4	8.88	308	1357	45.2	39	6.65	1.51	5.22	1.96
13	278	55	206	3.7	7.71	280	1049	39.3	38	5.51	1.47	4.29	1.88
14	287	67	337	5.1	10.17	339	1714	51.8	52	7.92	1.57	5.62	1.91
15	394	32	229	7.2	8.64	163	1166	44.0	31	11.89	1.66	8.06	1.99
16	400	113	402	3.6	9.64	576	2047	49.1	46	4.19	1.18	4.21	1.90
17	407	35	144	4.1	7.29	178	733	37.1	36	7.73	1.88	4.91	1.95
18	417	59	245	4.2	8.55	300	1248	43.5	40	6.31	1.52	4.98	1.96
19	483	60	264	4.4	8.28	306	1345	42.2	33	5.82	1.32	5.10	1.93
20	663	90	425	4.7	10.49	458	2165	53.4	47	6.23	1.32	5.44	1.94
21	687	19	76	4.0	3.90	97	387	19.8	14	4.07	1.02	4.84	1.96
22	709	23	106	4.7	4.74	115	537	24.1	27	5.08	1.08	5.60	1.98
23	716	25	89	3.6	4.61	127	453	23.5	22	4.33	1.22	3.84	1.80
24	725	25	101	4.0	5.09	127	514	25.9	20	5.27	1.31	4.80	1.94
25	733	45	204	4.5	7.32	229	1039	37.3	38	6.07	1.34	5.29	1.95
26	810	25	156	6.3	7.17	125	792	36.5	37	10.69	1.68	7.27	1.99
27	889	32	99	3.1	3.71	163	504	18.9	19	2.19	0.71	3.56	1.83
28	895	14	40	2.9	3.12	71	204	15.9	12	3.54	1.24	3.43	1.85
29	904	54	151	2.8	4.18	275	769	21.3	24	1.65	0.59	3.30	1.82
30	951	45	129	2.9	6.25	229	657	31.8	27	4.43	1.54	2.89	1.66
31	958	45	132	2.9	5.46	229	672	27.8	24	3.37	1.15	3.02	1.69
32	997	41	131	3.2	7.29	209	667	37.1	28	6.60	2.07	3.56	1.80
33	1006	2	10	5.0	0.62	10	51	3.1	6	0.97	0.19	5.00	1.80
34	1013	74	212	2.9	6.44	374	1077	32.8	28	2.87	1.00	3.21	1.77
35	1023	38	87	2.3	3.55	191	441	18.1	15	1.71	0.74	2.13	1.49